

# Scramjet test flow reconstruction for a large-scale expansion tube, Part 1: quasi-one-dimensional modelling

D. E. Gildfind<sup>1</sup> · P. A. Jacobs<sup>1</sup> · R. G. Morgan<sup>1</sup> · W. Y. K. Chan<sup>1</sup> · R. J. Gollan<sup>1</sup>

Received: 1 April 2017 / Revised: 29 October 2017 / Accepted: 8 November 2017 / Published online: 29 November 2017  
© Springer-Verlag GmbH Germany, part of Springer Nature 2017

**Abstract** Large-scale free-piston driven expansion tubes have uniquely high total pressure capabilities which make them an important resource for development of access-to-space scramjet engine technology. However, many aspects of their operation are complex, and their test flows are fundamentally unsteady and difficult to measure. While computational fluid dynamics methods provide an important tool for quantifying these flows, these calculations become very expensive with increasing facility size and therefore have to be carefully constructed to ensure sufficient accuracy is achieved within feasible computational times. This study examines modelling strategies for a Mach 10 scramjet test condition developed for The University of Queensland's X3 facility. The present paper outlines the challenges associated with test flow reconstruction, describes the experimental set-up for the X3 experiments, and then details the development of an experimentally tuned quasi-one-dimensional CFD model of the full facility. The 1-D model, which accurately captures longitudinal wave processes, is used to calculate the transient flow history in the shock tube. This becomes the inflow to a higher-fidelity 2-D axisymmetric simulation of the downstream facility, detailed in the Part 2 companion paper, leading to a validated, fully defined nozzle exit test flow.

**Keywords** Expansion tube · Scramjet · Free-piston driver · Computation fluid dynamics · Quasi-one-dimensional

---

Communicated by Z. Jiang and A. Higgins.

✉ D. E. Gildfind  
d.gildfind@uq.edu.au

<sup>1</sup> The University of Queensland, St. Lucia, QLD 4072, Australia

## 1 Introduction

Free-piston driven expansion tubes are uniquely capable of reproducing the flight conditions associated with return to Earth from deep space, flight into the atmospheres of the other planets, or scramjet-powered access to space. Their test gas is produced by a series of impulsive flow processes which involve complex and unsteady wave processes, and viscous and high-temperature gas effects. To make proper use of their capabilities, it is necessary to accurately characterize the test gas properties, both spatially and transiently. However, it is exceedingly difficult to directly measure many of the final test flow properties, especially on a routine basis.

Computational fluid dynamics (CFD) analysis of the facility therefore plays an important role in reconstructing the experimental test flow. These simulations reproduce part or all of the experiment and must account for all important flow processes from the moment the piston is released to when the last of the useful test gas has passed through the test section. The full-scale facility geometry is simulated time-accurately in order to account for transient wave processes. Furthermore, the grid spacing needs to match instrumentation length scales in order to adequately resolve transient flow properties for comparison with these high-frequency experimental diagnostics, such as tube wall static pressure traces, shock speeds, and pitot pressure traces. This results in large calculations which increase rapidly with facility size; the number of grid cells increases with tube length and diameter; furthermore, the simulation must be run for longer, since flow processes in a physically larger facility take longer to complete.

The University of Queensland's (UQ's) free-piston driven X3 facility ([1]; Fig. 1) is the largest facility of its type in the world. By virtue of its size and total pressure capability, X3 is ideally suited to extend ground testing of scramjet engine

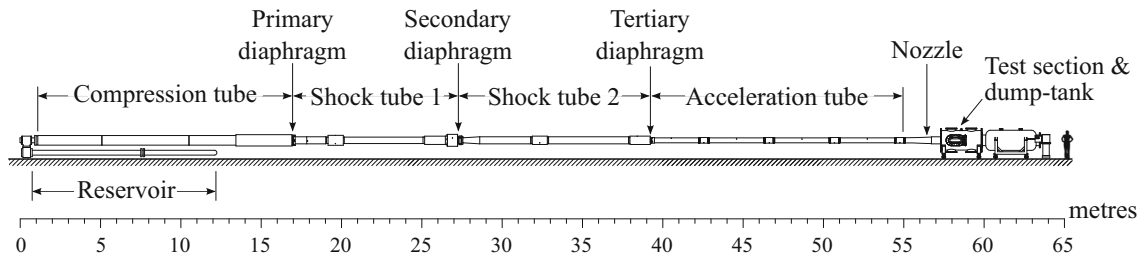


**Fig. 1** University of Queensland's X3 expansion tube facility (to scale), 2013 configuration. Supporting carriage work, pressure manifold, and associated hardware, are not shown

technology well beyond the current Mach 10, 50 kPa dynamic pressure limit of reflected shock tunnels. Recent scramjet combustion testing at Mach 10 has validated the facility's potential for this type of testing [2], and efforts are currently well progressed towards conducting the first ever free-stream engine testing at Mach 12 [3]. However, for a facility of X3's size, fully resolved CFD calculations can become impractically large, exceeding millions of processor hours. Looking ahead to future testing, there is a pressing requirement to develop a practical but reliable analysis framework to characterize the various new test flows which the facility will generate.

This paper reports on the first stage of a study to reconstruct a recent X3 Mach 10 scramjet flow condition, first reported in Ref. [4], which is representative of the types of scramjet test flow the facility will be used for into the future. As discussed in Sect. 5, a hybrid 1-D/2-D CFD analysis methodology is currently used to compute expansion tube test flows. Using this methodology, computationally expensive, time-accurate, two-dimensional axisymmetric CFD is used to simulate the low-density downstream part of the facility, during the final stage of the experiment (for this study, the final 10 ms), during which the test gas flows across this low-density region into the test section. The transient inflow to this 2-D model is computed using a quasi-one-dimensional CFD analysis of the *entire* facility, including the free-piston driver, for the entire duration of the experiment (180 ms), at comparatively insignificant computational cost.

Construction of the 1-D model directly influences the accuracy of the final computed 2-D test flow. However, its reduced dimensionality means that complex 2-D and 3-D processes must be accounted for through the use of engineering correlations, and by adjustments to the model configuration, both of which are tuned against shock speeds and static pressures measured during an actual experiment. Limited guidance is available on this tuning process; however, as this paper demonstrates, the characteristics of the computed flow are fundamentally affected by it. This paper first presents the background and details of the hybrid modelling process and describes the experimental configuration for these X3 Mach 10 experiments. It then provides a detailed

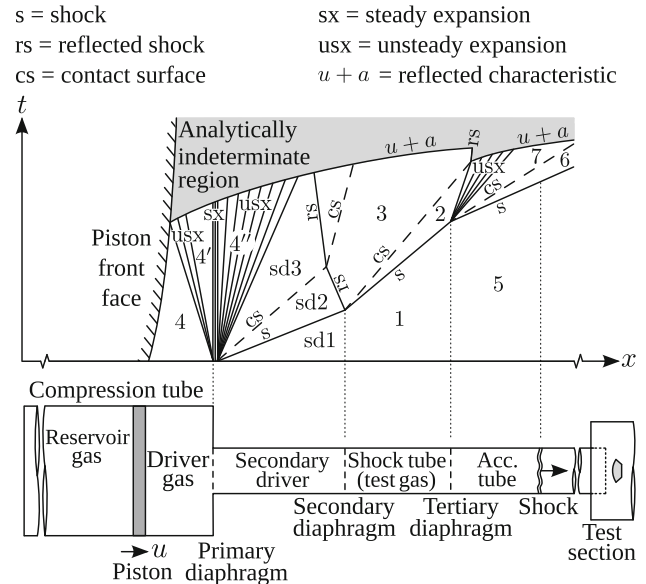


**Fig. 2** Idealized  $x-t$  diagram for expansion tube operation with a secondary driver. Acc. refers to Acceleration. Adapted from [5]

examination of the 1-D analysis process, leading to identification of the most effective modelling techniques.

## 2 Expansion tube operation for scramjet testing

Figure 2 shows the primary wave processes arising inside a free-piston driven expansion tube operating with a shock-heated secondary driver, which has been the configuration used for high Mach scramjet tests at UQ [2,5]. A detailed discussion of the secondary driver operating mode can be found in Refs. [6,7].

Referring to Fig. 1, the test gas is initially contained in the long steel "shock tube 2", sealed between the thin Mylar secondary and tertiary diaphragms. Upstream of the secondary diaphragm is the secondary driver (termed "shock tube 1"), initially filled with helium and separated from the larger-diameter free-piston driver by a steel primary diaphragm. The compression tube contains a free-sliding heavy piston and a light driver gas comprised of helium and argon. On the

downstream side of the tertiary diaphragm is the long acceleration tube which extends to the test section and is initially at low pressure (typically of order 10 or 100 Pa for high Mach scramjet testing).

When the facility is fired, compressed air accelerates the piston into the driver gas, which it compressively heats until the increasing pressure ruptures the primary diaphragm. The hot, high-pressure driver gas drives a strong shock through the helium secondary driver gas, accelerating it downstream. The secondary driver is configured in an over-tailored condition, such that the sound speed of the shock-heated secondary driver gas exceeds that of the expanded driver gas driving it, and is configured this way to prevent transmission of noise from the primary driver directly to the test gas [7–9]. When the shock wave arrives at the secondary diaphragm, the lower density helium gas decelerates upon impacting the higher density air test gas, which occurs through a reflected shock. The primary shock is transmitted to the test gas, which itself is compressively heated and accelerated downstream. Prior to arriving at the test section, the shock-processed test gas passes into the low-pressure acceleration tube. The forward portion of the gas is expanded up to flight conditions through an unsteady expansion, which dramatically increases its enthalpy and total pressure. Since this occurs at high speed, the static temperature and pressure never reach stagnation levels, and it is possible to create chemically-correct test flows at extremely high flight enthalpies and total pressures.

The test time begins when the expanded test gas arrives at the test section; it ends when the flow properties depart too far from their baseline values, which typically occurs well before the trailing driver gases arrive. In a large facility such as X3, the test duration can vary between hundreds of microseconds to over one millisecond, depending on the simulated flight speed and other test flow parameters.

### 3 Test flow reconstruction

The operation of expansion tubes poses two major challenges. The first challenge has been to show that it is, indeed, possible to configure these complex machines to produce test flows at the desired conditions. So far, the overwhelming effort in expansion tube research has been directed towards establishing proof-of-concept—showing that these facilities actually work—and this first challenge has largely been met [5, 8, 10–13].

The second challenge is to accurately define the full test flow properties. To make sense of their experimental measurements, experimentalists must know exactly what flow is passing over their planetary entry heat shield model, or exactly what flow is passing into their scramjet inlet. However, characterizing the impulsive and extremely short duration test flows which these expansion tubes produce is

a difficult and complex problem in itself, and this second challenge has not yet been fully addressed. For example, considering UQ's X2 and X3 expansion tubes, while it is now possible to routinely generate a wide range of unique test conditions, quantifying and characterizing each of these conditions to a high level of accuracy remains very challenging.

This second challenge is made more urgent by the continuing advances in hypersonics research; designers and researchers need increasingly more precise experimental measurements to continue to improve maturing physical models and CFD codes, and to differentiate between the performance of different designs. For example, the operation of a scramjet-powered vehicle at high Mach numbers requires a very fine balance between the forces of thrust and drag within a complex 3-D flow field, and approximate measurements and computations are simply not adequate.

Test flow reconstruction involves quantifying relevant test flow properties, such as static pressure, temperature, velocity, and test flow chemistry. In X3, the experimenter needs to know how these properties vary across the nozzle exit plane, as well as longitudinally into the test section. Only a central core of the test flow is not compromised by boundary layer effects; this region is termed the core flow and is defined by a diameter measurement. Furthermore, in an expansion tube it is important to be able to quantify how these properties change with time.

Directly measuring expansion tube flows is extremely difficult. Test times are very short (around 1 ms for a large facility such as X3), and the expansion tube presents an extremely harsh instrumentation environment. Only a limited range of routine measurements are possible: contact measurements include static pressures along the tube walls (which also permit calculation of the average speeds of the shock between transducers) and Pitot/impact pressures across the nozzle exit. Thus only a limited dataset of localized pressure measurements and shock speeds are typically available, and these by themselves are insufficient to adequately describe the test flow.

Understanding and quantifying the full extent of facility flow processes is important for the design and optimization of expansion tube test conditions. However, in terms of the experiment itself, the only flow properties which really are of interest are those *downstream* of the nozzle exit plane, in the region where the scramjet experiment takes place, and ideally these properties would be directly, precisely, and completely characterized through experimental measurement. Upstream flow properties become relevant only when this additional information is necessary to reconstruct the full test flow property set.

Numerical analysis is used to bridge the gap between the *actual* test flow, which is of interest, and the *known* data about the facility flow processes, which may reside at other

locations in the facility. Since numerical analysis always, to varying degrees, relies on simplifying assumptions, discretization error, imprecise boundary conditions, and since it does not completely capture all of the physical processes of the system, uncertainties cascade across regions of the facility which are modelled by this process. As a general principle, therefore, it is desirable to minimize the gap between the *known* inputs and the *desired* outputs (in this case, the transient and spatial characteristics of the test flow). Furthermore, since available computing power will continue to limit the fidelity of numerical simulations into the foreseeable future, it is necessary to carefully allocate available computing resources to critical parts of the problem at hand.

Given the difficulty with making experimental measurements of the final test flow properties, significant analytical and numerical analysis of the *entire* facility is required in order to estimate the eventual test flow properties. To illustrate the complexity of this problem, it is instructive to first compare an expansion tube nozzle flow to that of a reflected shock tunnel (RST). At the inlet to an RST nozzle, the test gas is stagnated by a reflected shock, and stagnation pressure transducers not only provide measurements of the stagnation pressure, but can also be used to determine the primary and reflected shock speeds. These three properties can be used to estimate the stagnation temperature.

The stagnated test gas then undergoes a steady expansion from reasonably well-defined initial conditions through to the nozzle exit. A steady flow from the nozzle exit results, which is preceded by a nozzle start-up process and concludes when driver gas contamination becomes excessive. Considering some well-established facilities, such as T4 in Brisbane, or The High Enthalpy Shock Tunnel Göttingen (HEG), the test flow properties are reconstructed by performing a steady 2-D axisymmetric CFD calculation of the nozzle and part of the test section, assuming a constant nozzle inflow at the measured/calculated stagnation condition [14, 15]. These calculations can be performed on a resolved grid in a matter of hours using a block-marching technique, have associated Pitot pressure distributions which match experimental measurements well, and provide a practical basis for routine experimentation [14].

In contrast to the RST, an expansion tube nozzle has a fundamentally unsteady, non-uniform inflow, characterized by the passage of several different flow stages:

1. A relatively brief burst of hot, low-density accelerator gas;
2. The accelerator/test gas interface;
3. The unsteadily expanded portion of test gas, followed by the unsteady expansion itself;
4. The secondary driver/test gas interface;
5. The secondary driver gas;
6. The primary driver/secondary driver gas interface;

7. The primary driver gas;
8. Significant amounts of fragmented Mylar are also distributed through these gases, which no 2-D modelling techniques currently account for.

Considering just the expansion tube nozzle, in order to adequately predict the properties of the useful test gas which is produced at the nozzle *exit* by this process, it is necessary to transiently define a sufficient portion of the upstream nozzle *inflow*, which must often include flow stages up to and including the secondary and primary driver gases. Furthermore, since the passage of the accelerator and test gases along the length of the driven tube normally introduces significant viscous effects, for an axisymmetric facility it is necessary to supply the *radial* variation in these inflow flow properties to the nozzle.

Compared to an RST, an expansion tube nozzle calculation therefore suffers from both a transiently and spatially variable inflow which cannot be readily defined by routine experiment and calculation, and furthermore, must be computed by fully unsteady CFD calculation. The problem has orders-of-magnitude greater computational requirements, which is compounded by considerably more difficult-to-define inflow conditions. Both of these factors make it very difficult to produce practical, routine, but satisfactory estimates of test flow properties to support experimentation with these facilities. The objective of this study is to address the challenge this presents.

## 4 Experimental set-up

The X3 facility, shown in Fig. 1, is the world's largest free-piston driven expansion tube. It has a 14.5-m-long, 500-mm-internal-diameter compression tube, a 40-m-long driven tube and nozzle, and a large volume test section and dump tank. Its high-pressure compressed air reservoir is located underneath the compression tube. The detailed geometric layout of X3 is shown in Fig. 3; more details on the facility can be found in Ref. [6].

Referring to Fig. 3, ct, st1–st7, and at1–at8 are locations of fast response piezoelectric PCB(R) pressure transducers. These are mounted flush to the tube wall and measure static pressure of the flow; ct is located in the compression tube and provides a measurement of the driver pressure. Transducers st1–st4 are located in the first driven tube section, which was used as a secondary driver for these experiments; st5–st7 are in the second driven tube section, which contained the test gas; at1–at8 are located in the third tube section, which is the low-pressure acceleration tube. Tube wall pressure transducers measure the static pressure of the passing flow; shock arrival at each transducer is also used to calculate average



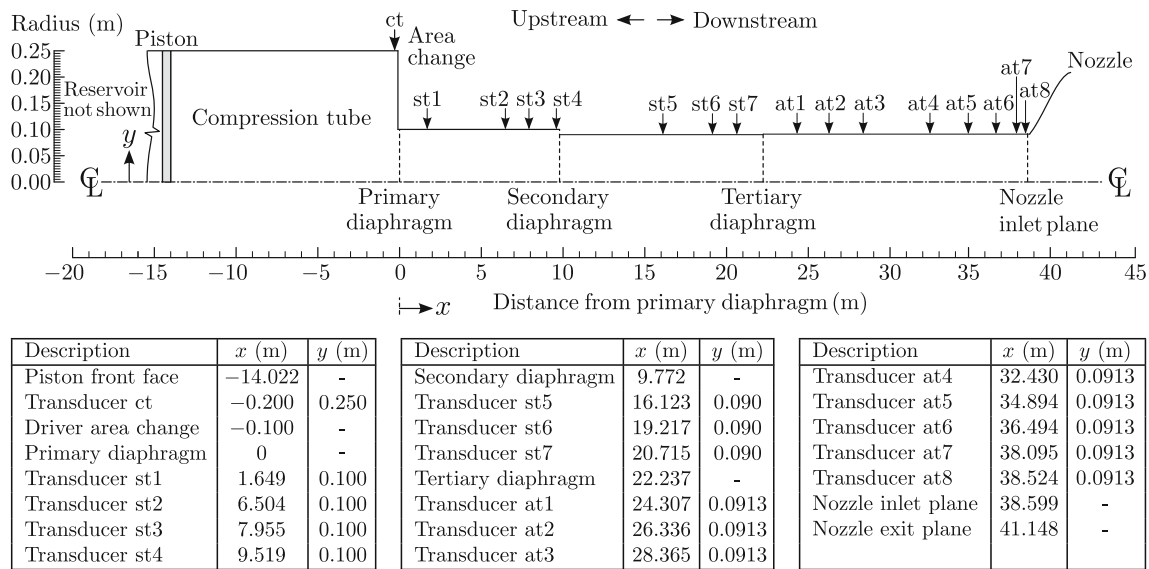


Fig. 3 Geometric layout of X3 expansion tube facility, 2013 configuration. Longitudinal scale compressed for clarity. Adapted from [16]

time-of-flight shock speeds between adjacent transducers, which is an important metric for CFD validation.

For these experiments, an instrumentation rake was installed at the nozzle exit (Fig. 4). Flow surveys were performed with the forward tip of the Pinckney probe positioned at 80, 292, and 550 mm aft of the nozzle exit plane. Referring to Fig. 4,  $13 \times 15^\circ$  half-angle cone probes (described in Ref. [17]) measured static pressure at the cone surface (instrumented with robust PCB(R) 112-A22 piezoelectric pressure transducers). These were used to make a partial impact measurement similar to the Pitot pressure. However, unlike a Pitot probe, which always develops a normal shock in supersonic flow, the cone probe processes the flow with a conical shock. The angle of the conical shock depends on the Mach number and the ratio of specific heats; therefore, the Mach number cannot be directly calculated from the cone probe impact pressure and free-stream static pressure. However, at high Mach numbers the conical shock angle becomes reasonably insensitive to Mach number (asymptoting to a fixed angle for  $M \rightarrow \infty$ ), and an equivalent metric can be calculated from the CFD simulation to permit comparison. The CFD calculation also takes into account high-temperature effects with its equilibrium chemistry model, based on computations using the NASA CEA code [18]. Their conical shape means that these probes are subject to much lower heating and pressure loads than Pitot probes, and their small forward cross section means they present a smaller obstacle to debris entrained in the flow (such as Mylar diaphragm fragments). Furthermore, experience with X2 and X3 has shown that they can provide steadier pressure measurements than conventional Pitot probes in these scramjet flows.

The upper probe in Fig. 4 is a Pinckney probe [19], designed to measure test flow static pressure, and comprises a

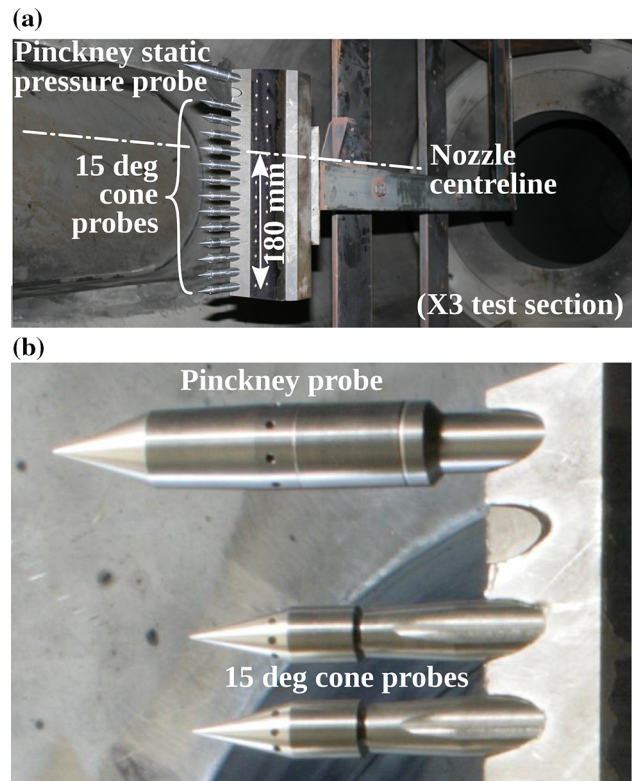


Fig. 4 X3 Pitot rake configuration; a general set-up; b close-up view of probes. Adapted from [4]

$20^\circ$  cone, a  $2^\circ$  ramp, followed by a cylindrical surface parallel to the free-stream. After conical shock processing over the  $20^\circ$  cone, the test flow is twice expanded, and pressure is then measured on the cylindrical surface. Ignoring viscous effects, the test flow should eventually expand to the free stream

static pressure. However, in practice the measured pressure depends on several factors, including the length of the probe and the effects of viscosity, which can be accounted for with CFD analysis of the probe at the specific flow condition. The Pinckney probe was instrumented with a 10 psi Kulite XTEL-190 piezoresistive pressure transducer. The Kulite produces a continuous and low-noise signal, but is less robust than the PCB and cannot tolerate significant overpressure. However, it could be used in this application since the transducer was well protected from impacting debris, and the maximum absolute pressure downstream of the two expansion ramps was within the limits of the transducer.

Note that all experimental pressure traces in this paper and its companion Part 2 paper [20] have been filtered with a low-pass Butterworth filter (100 kHz for the PCB 112-A22; 50 kHz for the Kulite XTEL-190). These frequencies are less than the natural frequencies of the sensors (250 kHz for the PCB [21] and 175 kHz for the 10 psi Kulite [22]) and were found to provide a relatively clean signal whilst retaining the significant transient details of the trace.

#### 4.1 Flow condition

The flow condition examined in this paper was originally developed for Mach 10 scramjet combustion testing in X3, at flight dynamic pressures relevant to a realistic access-to-space ascent trajectory. The facility configuration for these experiments is detailed in Table 1, and the flow condition is identified as “x3-scr-m10p0a-rev-0”. For these experiments, the driver was operated with a 200-kg piston and an orifice plate at the driver area change. The first section of driven tube was configured as a shock-heated secondary driver and operated in over-tailored mode to prevent ingress of driver

**Table 1** X3 Mach 10 scramjet flow condition “x3-scr-m10p0a-rev-0”

Property	Value
Reservoir fill pressure	3.8 MPa
Piston mass	200 kg
Driver fill pressure, $p_{4,0}$	30 kPa
Driver gas composition, by partial pressure	60% He/40% Ar
Driver orifice diameter	149 mm
Primary diaphragm	2.0-mm cold-rolled steel
Diaphragm rupture pressure	17.5 MPa ( $\lambda = 45.7$ )
Secondary driver fill pressure, $p_{sd,1}$	70 kPa (He)
Secondary diaphragm	0.1 mm Mylar
Shock tube fill pressure, $p_1$	39 kPa (air)
Tertiary diaphragm	0.1 mm Mylar
Acceleration tube fill pressure, $p_5$	120 Pa (air)

flow disturbances to the test gas. The full rationale for using this operating mode with scramjet flow conditions is detailed in Ref. [6], which provides a general discussion on the use of secondary drivers to increase shock strength and improve test flow quality in expansion tubes. The shock and accelerator tubes were filled with air at 39 kPa and 120 Pa, respectively.

In the process of developing the new condition, a number of experiments were conducted. Once the detailed operating parameters had been established, five repeat experiments were performed. Tube instrumentation was constant between shots; however, the nozzle instrumentation rake position was varied. The six experiments (labelled x3s403 and x3s410 to x3s414) demonstrated excellent repeatability. Shot x3s403 was the first shot at this condition and is therefore used throughout this paper as the reference experimental condition for CFD comparisons with tube experimental diagnostics.

## 5 Hybrid CFD analysis

Two-dimensional axisymmetric simulation is currently the highest fidelity practical technique available to model impulse facility flow processes. At UQ, these simulations are performed using the in-house Eilmer3 code, which is a 2-D/3-D Navier–Stokes compressible flow solver [23]. The code implements an explicit updating scheme and is therefore time-accurate, includes equilibrium and finite rate chemistry models, and Baldwin–Lomax and  $k-\omega$  turbulence models.

However, the high computational cost currently makes it impractical to perform a full 2-D axisymmetric analysis of a large free-piston driven expansion tube such as X3. At UQ, a hybrid modelling technique is adopted, whereby the facility is first simulated using the quasi-one-dimensional Lagrangian solver L1d [24]. L1d calculates the full facility response across the entire duration of the experiment, commencing at piston launch. It accurately captures all of the longitudinal wave processes and includes the piston dynamics. The primary function of L1d is to calculate a time-accurate inflow to the low-pressure acceleration tube, both rapidly and at low computational expense. A high-fidelity 2-D axisymmetric simulation is then performed for the low-pressure acceleration tube, nozzle, and test section, providing the final test flow.

There are several reasons why the hybrid modelling technique is used for this type of analysis. Firstly, it reduces the grid size; referring to Fig. 3, the size of the flow domain is reduced by approximately two-thirds by confining the upstream boundary of the 2-D simulation to the st6 transducer location, just upstream of the acceleration tube (which begins at the “tertiary diaphragm” in Fig. 3). Furthermore, the hybrid technique dramatically reduces the costly axisymmetric simulation time; considering the Mach 10 operating condition described in this paper, after the piston is launched

it takes approximately 163 ms for the primary shock wave to reach st6, at which point the axisymmetric simulation begins. This entire preliminary process is simulated time-accurately at insignificant computational cost using L1d. By modelling flow processes downstream of st6 only, the required 2-D axisymmetric CFD simulation time is reduced from 173 ms, (i.e.,  $163 + 10$ ), to just 10 ms.

Confining the axisymmetric calculation to the downstream end of the facility is justified on the grounds that viscous effects generally only become significant in the low-pressure acceleration tube, where they can produce thick boundary layers which can significantly impact the test flow core diameter and cause shock wave attenuation through the “Mirels” effect [25,26]. The hybrid methodology applies the high-fidelity 2-D axisymmetric analysis to this low-pressure flow domain, thereby capturing the important viscous phenomena. However, these effects are less influential in the higher density shock tube and driver, and therefore, L1d can be used for these parts of the facility.

The use of a 1-D solver in the hybrid scheme also facilitates modelling of the piston dynamics, which are more readily modelled in the Lagrangian (moving cell) L1d solver. Using a 2-D grid would require moving grid capability as well as a time-accurate measurement of the piston trajectory (although this capability is being introduced in the next version of the code, Eilmer4).

Finally, tuning of the CFD model is required in order to replicate measured experimental diagnostics as closely as possible. The L1d simulations are sufficiently small in terms of computational cost that iterative tuning is practical and straightforward, whereas it is computationally too expensive to apply the same approach to large 2-D axisymmetric simulations.

Early attempts at hybrid modelling applied a steady, radially uniform inflow to the acceleration tube [27,28]. Normal shock relations were used to calculate the test gas flow properties based on experimentally measured shock speeds. This approach assumes the ideal set of wave processes shown in Fig. 2 and does not account for transient changes in the test gas properties due to more complex upstream wave processes. It is therefore most suitable for high enthalpy conditions (for example,  $H_s > 25$  MJ/kg) where wave process coupling is less significant.

More recent studies of high enthalpy test flows [29–31] have used L1d to calculate a transient, radially uniform inflow to the acceleration tube. Reference [5] used the same approach for high density scramjet test flows; however, the axisymmetric analysis was extended to include part of the shock tube, and the radially uniform inflow was modified to include an estimate of the turbulent boundary layer development.

Eilmer3 has previously been used to simulate the entire X2 expansion tube facility [17]. In this study, X2’s free-piston

driver was modelled as a fixed volume with initially uniform pressure and temperature. The driver was made sufficiently long that reflected driver expansion waves would not significantly affect downstream flow processes during the test time, thereby replicating the quasi-steady driver gas supply of X2’s tuned free-piston driver [32]. This model was used to identify sources of flow disturbances and loss mechanisms in the driver and revealed a total pressure loss region due to a complex shock train which develops downstream of the primary diaphragm. This type of model is less well suited to the task of accurate test flow reconstruction for two reasons: firstly, the transient behaviour of the free-piston driver is not accounted for; secondly, compared to a 1-D facility model, the large computation time of a 2-D model (or order 10,000–100,000 CPU hours) makes it unsuitable for iterative fine-tuning to match the exact performance observed in the experiment.

A three-stage hybrid CFD scheme was used for the present study and is shown in Fig. 5. Specific parameter values, such as cell count and calculation time, represent the final tuned CFD calculations.

The first stage involved simulating the entire facility in 1-D using L1d. The simulation was tuned to match two experimental measurements: driver pressure vs. time and the shock speed between the most downstream pair of transducers in the shock tube, st6 and st7. Viscous and inviscid models were developed, which are detailed in Sect. 6. The flow history at the st6 axial location was recorded for use as an inflow to the axisymmetric model. The total L1d simulation time was 180 ms; the useful inflow from st6 occurred between approximately 163–173 ms.

The second stage of the hybrid scheme involved 2-D axisymmetric CFD analysis. A structured grid model was constructed for the driven tube downstream of the st6 axial location and was developed to calculate the transient and radially variable inflow to the nozzle inlet. The L1d st6 flow history was used for two different types of inflow to the tube model at st6: firstly, as a radially uniform inflow; secondly, as a radially uniform inflow modified to include a boundary layer in accordance with the methodology detailed in Refs. [5,17]. Although the tube model included the nozzle and first 1 m of the test section, the structured grid resulted in a large increase in the radial grid spacing through the diverging nozzle. This model was therefore used only to calculate the radially non-uniform nozzle inlet flow at the downstream end of the acceleration tube.

The third stage of the hybrid scheme involved 2-D axisymmetric CFD of the nozzle and test section. To achieve equivalent grid refinement through these two sections, a separate model was developed, using the 2-D nozzle inflow history from the tube axisymmetric model. This refined grid provided the final test flow properties for the hybrid simulation.

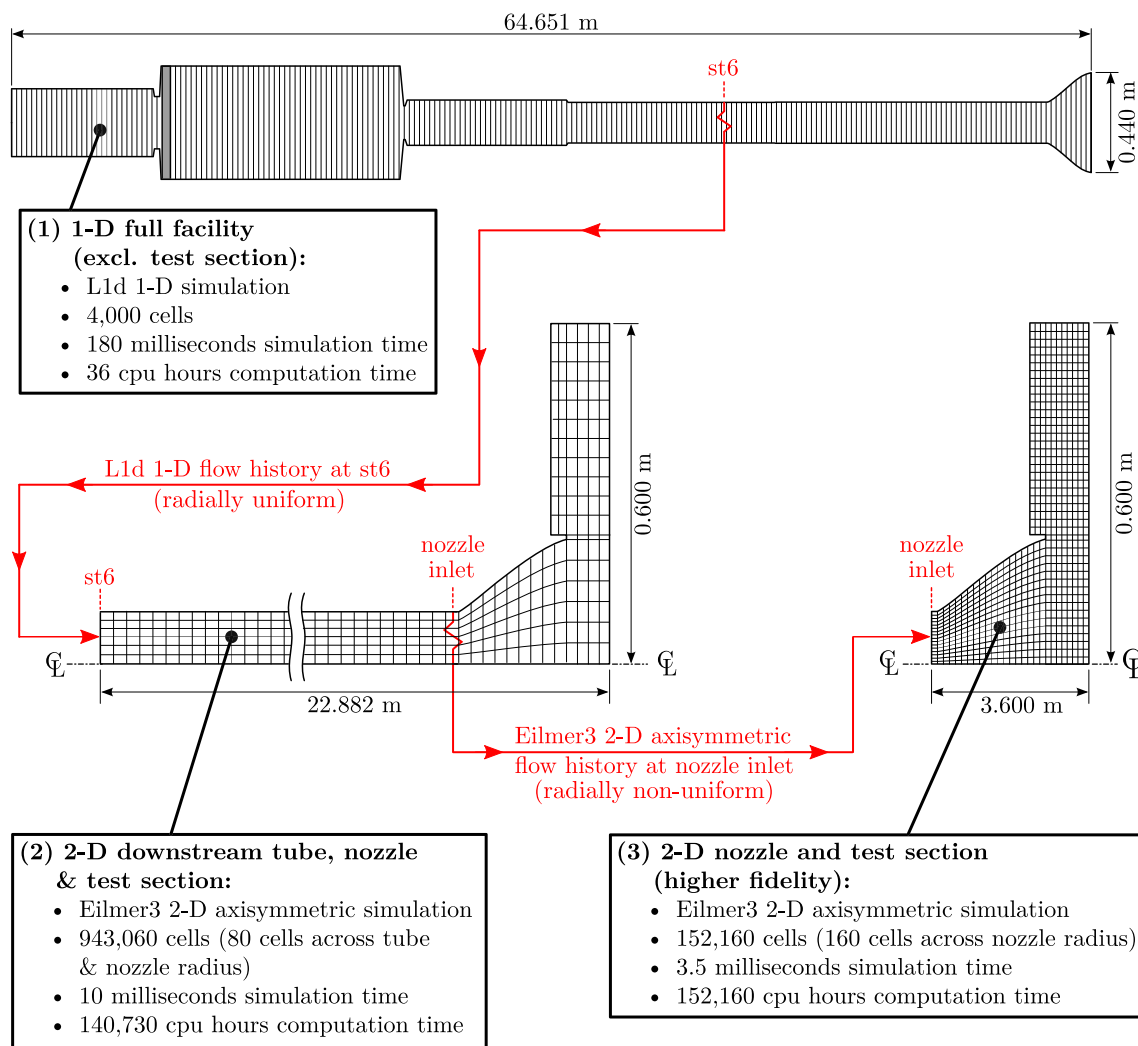


**Fig. 5** Hybrid CFD scheme. Longitudinal scaled compressed

The first stage of the hybrid scheme (the L1d modelling) is presented in this paper; the most effective L1d model is shown to give good estimates of the shock speeds in the secondary driver and shock tube, to accurately compute the transient flow history in the shock tube, and avoids any spurious flow features within the flow field. However, L1d cannot accurately predict the properties of the expanded test flow at the nozzle exit. The remaining two stages of the hybrid scheme are presented in the Part 2 companion paper [20] and yield the validated, fully defined (both transiently and spatially) nozzle exit test flow.

## 6 Quasi-one-dimensional facility CFD

### 6.1 The L1d code

L1d is a quasi-one-dimensional Lagrangian CFD code designed to simulate free-piston driven impulse facilities

[24]. The full source code is available online under the GNU Public License from The Compressible Flow CFD Project at UQ [33]. The explicit solver calculates the time evolution of internal flow processes in the facility, beginning at piston launch. Gas slugs along the length of the tube are discretized, axially, into fixed-mass cells that slide within the varying-area tube. Each cell spans the full local diameter of the tube, and boundary effects, such as heat transfer and wall friction, are permitted at the wall boundary of each cell. Beyond the fixed-mass nature of the cells, the conservation equations for axial momentum and energy are applied to each cell. The cell data are assigned to the cell centre and, for each time step, are interpolated to the interfaces between adjacent cells. There, an approximate Riemann solver [34] is used to compute the pressure and gas velocity, which then is used in conservation equations to compute the rate of change of cell momentum and energy. Piston dynamics are calculated from the pressure difference acting across the piston and can account for piston



friction. Pipe flow engineering correlations are used to estimate viscous effects and complex 2-D/3-D flow processes [35].

The simulation code uses these numerical methods to simulate the axial wave motions that are the primary driving processes within an expansion tube facility; however, a consequence of the one-dimensional nature of the discretization is that there are two significant modelling limitations. First, the code can accommodate only gradual changes in duct area. Area transitions that are characteristic of the expansion tube facilities need to occur over distances that are large relative to the length of the cells moving through the area changes. The minimum distances needed for the area transitions may be reduced with increasing resolution of the gas slug discretization.

A second, more subtle, limitation is that there is no internal distinction between core flow and boundary layer within each cell. This means that the boundary effects, such as wall friction and heat transfer, manifest directly as changes to the core flow conditions. This instantaneous effect on core flow conditions is not physically correct and leads to modelling uncertainty that cannot be fixed simply with increased resolution. However, it is a secondary effect that does not usually overwhelm the accurate capture of the axial wave motions. Where this error does become apparent is in the low-pressure regions of the facilities, especially towards the downstream end of the final expansion. There, the wall shear stresses become relatively strong and manifest as a computed axial pressure gradient within the fully expanded test gas. Also, in that region, the temperature of the core flow and the boundary layer should be greatly different. The instantaneous mixing within the computational cells reduces the accuracy of the simulated core flow conditions. These errors will be further noted in Sect. 6.3.

The code essentially performs a relatively rapid virtual experiment for the impulse facility. Converged calculations take from a few CPU hours to a few hundred CPU hours, depending on the size of the facility and the corresponding simulation time, i.e., the duration of the actual experiment. The principal advantage of L1d over analytical techniques is its ability to capture the full development of longitudinal gas-dynamic wave processes, including their interaction with the piston dynamics. This is particularly important for high density scramjet flow conditions, where wave processes are strongly coupled and therefore impractical to track analytically [5].

Another advantage of L1d is that the simulation can be tuned to improve the match between key experimental measurements and the corresponding parameters from the L1d calculation. Routine experimental measurements include tube wall static pressure traces and shock speeds based on time-of-flight between those transducers. This process must be applied with great care, but can be used to further correct the inflow to the axisymmetric simulation.

Figure 6 summarizes the L1d model used to perform the 1-D full facility simulation of X3. The reservoir is modelled in-line; however, it is located underneath the compression tube in the actual facility; see Fig. 1. ct, st1–st7, and at1–at8 represent actual transducer locations. All L1d simulations used equilibrium chemistry for the air test and accelerator gas regions (computed with NASA code CEA [18]). The air reservoir, helium/argon primary driver, and helium secondary driver, were all modelled with calorically perfect gas chemistry (viscosity calculated in accordance with Sutherland's law [35]). The initial temperature of gas regions was assumed to be 298.15 K. The experiment was simulated for 180 ms, which included the full piston stroke, and continued approximately 7 ms beyond the point when the useful

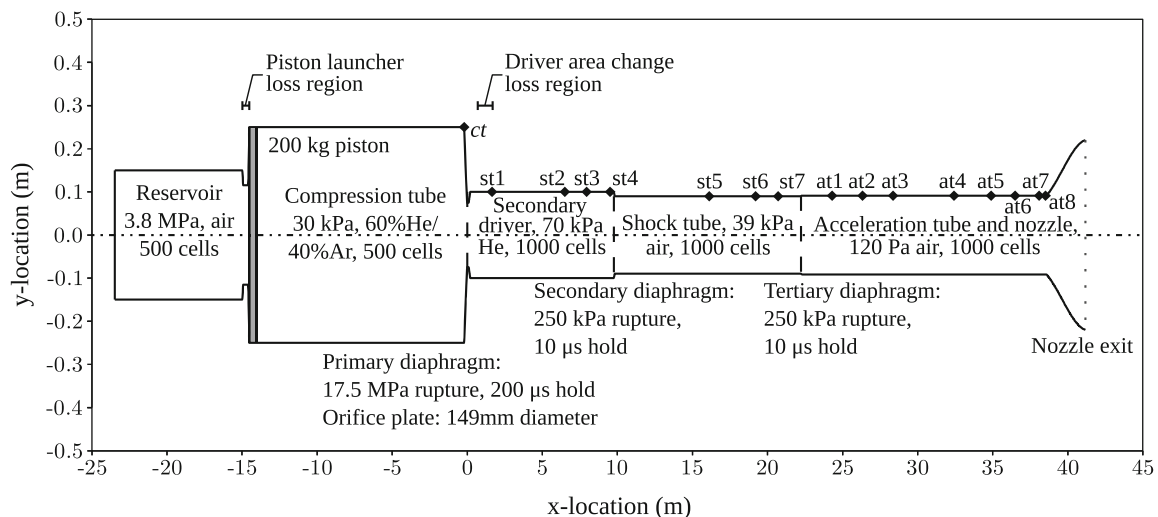


**Fig. 6** L1d geometric representation of the X3 impulse facility, with a nominal cell count of 4000

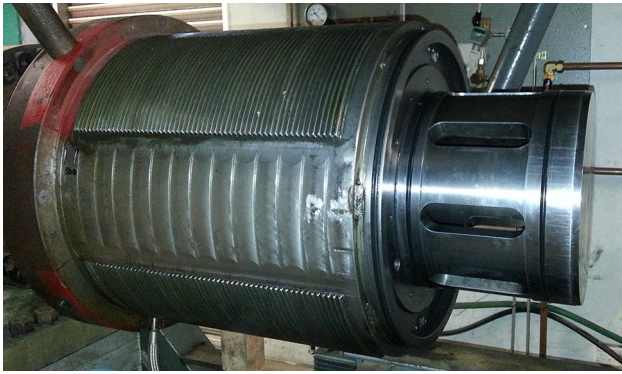


**Fig. 7** X3 piston launcher, which is located at the upstream end of the compression tube

test time had finished, as determined post-simulation. The grid described in Fig. 6, in terms of the number of cells axially, had the minimum cell density required to achieve a sufficiently grid-independent flow solution. See Sect. 8 for a formal assessment of the grid. Although the absolute computational cost of this model is low, at approximately 36 CPU hours for the inviscid model and 53 h for the viscous model, the model construction process is iterative. L1d currently runs on a single processor; therefore, longer calculation times become inconvenient and an efficient solution remains desirable.

Three important aspects of X3's true physical operation cannot be directly modelled in 1-D and require special treatment in the model. Firstly, referring to Fig. 1, X3's reservoir is located underneath the compression tube. Compressed air in the reservoir is turned through 180° before expanding through the slotted launcher to propel the piston. The slotted launcher is shown in Fig. 7. The piston initially slides over the slotted launcher, sealing the slots. Upon release, compressed air expands through the slots, propelling the piston down the compression tube. Referring to Fig. 6, despite the complex reservoir flow path in the actual facility, in L1d the reservoir must be modelled in-line with a single duct.

Secondly, discrete changes in duct area, such as the driver-to-driven tube area change, need to be modelled with a gradual area change.

Thirdly, complex flow paths, such as 3-D flow through the slotted launcher (Fig. 7), or the driver gas flow through the rupturing diaphragm, cannot be directly modelled. Pipe head "loss regions" are used to model associated losses in accordance with (1), where  $Q_{\text{momentum}}$  is incorporated into the momentum equation and has a nonzero value for any cell passing through the loss region [32, 35].  $\rho$ ,  $u$ ,  $A$ , and  $dl$  are, respectively, cell density, velocity, duct area, and cell length.  $K/L$  is the loss per unit length and must be determined from experimental data [32].

$$Q_{\text{momentum}} = -\frac{K}{L} \times \frac{1}{2} \rho u |u| \times A \times dl \quad (1)$$

L1d also has the option of modelling tube wall friction and heat transfer due to viscous effects, based on standard pipe flow correlations [35]. Viscosity is a binary option for each gas slug and cannot otherwise be configured.

## 6.2 Process for tuning the L1d model

Preliminary construction of the L1d model involves replicating the true facility configuration as closely as possible, without applying loss regions or tube wall viscosity. When the simulation is run, it will normally be found that the performance (in terms of driver pressure and temperature, and shock speeds achieved) is over-estimated, for four primary reasons.

In a free-piston driven facility, the first performance loss arises with the piston, which is propelled by compressed air initially contained in the reservoir. In X3, this air expands through a convoluted path from the lower reservoir, through a first set of internal slots where it is redirected to the upper compression tube and finally through the launcher slots into the space behind the piston. Significant total pressure losses occur during this process, and piston speeds observed during experiments are always significantly less than a baseline L1d simulation will predict.

The free-piston driver compression raises the temperature of the driver gas to several thousand Kelvin, and in the actual experiment there is heat loss to the tube walls, leading to the second performance loss. Recent driver spectroscopy of the current flow condition [36] indicated that the actual driver gas temperature reaches a peak of 3200 K, compared to 3750 K for an isentropic compression of the driver gas.

The third performance loss arises following diaphragm rupture, when the driver gas undergoes a strong expansion from the large diameter compression tube to the lower diameter shock tube. The gas is redirected by a series of oblique shock waves which induce a significant total pressure loss. Reference [17] analysed this process for the X2 facility, which is functionally identical to X3, using a 2-D axisymmetric CFD analysis and fixed volume approximation for X2's driver. Figure 8 (adapted from Ref. [17]) shows the X2 driver Mach number and static pressure 500  $\mu\text{s}$  after diaphragm rupture, and a complex shock train is evident. The driver is 80%He/20%Ar, the shock tube is helium, and the horizontal scale has been compressed for clarity. Total pressure loss through the driver area change was identified by Ref. [36] as the most likely source of reduced performance of X3's driver compared to analytical predictions (after driver gas spectroscopy eliminated heat loss as being the primary cause).

The fourth performance loss arises due to viscous effects in the driven tube, which cause shock attenuation and accelerate the test gas/accelerator gas interface due to the Mirels effect [25, 26].

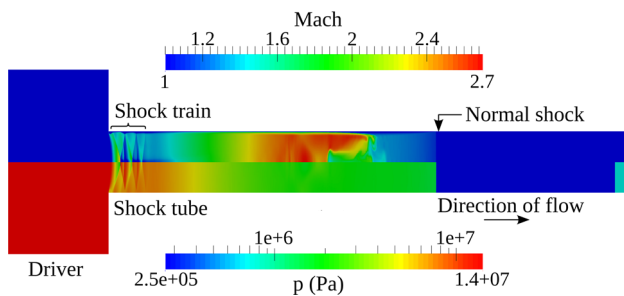


**Fig. 8** Shock train at driver area change for X2 Mach 10 flow condition, 500  $\mu$ s after the initiation of diaphragm rupture. Adapted from [17]

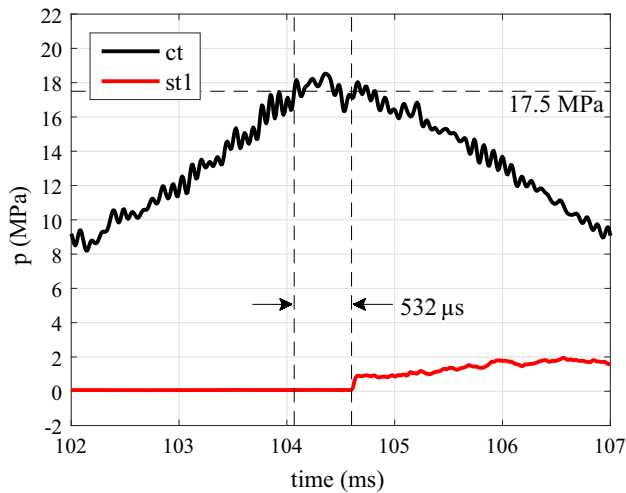


**Fig. 9** Shot x3s403 static pressures at transducer locations ct and st1

For the purposes of accurate test flow reconstruction, it is necessary to conduct the experiment before the L1d model can be tuned. In this context, L1d becomes a diagnostic tool (i.e., to determine what happened during the experiment), as opposed to a design tool (to develop new flow conditions). L1d model tuning is performed against two experimental measurements: driver pressure and shock speed.

Driver pressure is measured at transducer ct (see Fig. 6) and is shown in Fig. 9 (note: the original experimental time base is used). The static pressure trace at st1, which is 1.649 m downstream of ct, is also shown. Using the average experimental shock speed through the secondary driver of 3144 m/s, an approximate time between shock arrival at st1 and diaphragm rupture is 532  $\mu$ s. Noting that the ct pressure trace is measured at a location 0.2 m upstream of the primary diaphragm, the plot shown does not represent the actual pressure at the diaphragm face; however, it is indicative of pressure through this region of the driver. From the plot, it can be seen that the rupture time shown also corresponds to a change in the behaviour of the driver pressure curve. The average pressure after rupture is approximately 17.5 MPa and was used as the rupture pressure for the L1D model.

Shock speed is calculated from shock wave time-of-arrival, which can be measured at each tube wall static pressure transducer. Since the distance between each transducer is known, the shock wave average time-of-flight can be accurately calculated. An identical metric can be calculated in the CFD simulation. Typically the discrepancy between CFD and experimental shock speeds will vary along the tube; since this study used L1d to calculate an inflow at st6 for the 2-D axisymmetric model, the L1d tuning process targeted the shock speed between transducers st6 and st7.

These two experimental measurements—driver pressure and shock speed—provide only a limited insight into the complex expansion tube internal flow processes. The L1d tuning process aims to configure the 1-D simulation so that the computed driver pressure trace and st6–st7 shock speed match the experiment. However, the tuning process has to be performed with great care; improving the superficial agreement between L1d and experiment for these two measurements does not guarantee that the actual computed internal flow more closely represents the true state of the flow.

Previous studies with L1d have tuned simulations through the application of customized loss factors and have used L1d's viscosity option (for example, Ref. [37], which simulated the free-piston driven T-ADFA and T3 reflected shock tunnels (RSTs) in Canberra, the T4 RST in Brisbane, and the HEG RST in Göttingen; or Ref. [38], which simulated the HET fixed-volume driver expansion tube facility at the University of Illinois). As a first step, the present study has applied this technique to tuning the X3 L1d simulation (Sect. 6.3). However, recent experience with X2 and X3 facility simulations at UQ has indicated that using the viscosity model is problematic for expansion tubes, since the 1-D formulation introduces a strong but physically incorrect coupling between the boundary layer viscous effects and the core flow (discussed in Sect. 6.3). An alternative inviscid technique has been developed which uses a driver equivalent temperature based on Ref. [39] and avoids non-physical flow effects due to the viscosity model (Sect. 6.4). It is noted that both L1d models used equilibrium chemistry for the driven tubes. Results from the viscous and inviscid X3 simulations are compared to experiment in Sect. 6.5.

### 6.3 Viscous L1d simulation

For the viscous simulation, all gas slugs had the viscous option selected and were given an initial temperature of 298.15 K. Referring to Fig. 6, loss factors were applied at two locations. The first loss factor was applied along the piston launcher, for a length of 0.45 m; this was to account for pressure losses through the slotted launcher. The second loss factor was applied 0.7 m downstream of the primary diaphragm, over a 1.0 m length; this was to account for

heat and total pressure losses through the driver, before and after diaphragm rupture. This second loss region was placed well downstream of the primary diaphragm, since experience has shown that if a large loss factor is placed directly along the area change, which can be required to sufficiently “downgrade” the driver performance to match the observed experimental shock speeds, non-physical effects such as partial blockage of the duct can result.

The procedure to establish the extent and magnitude of loss factors is iterative and largely comes down to experience. However, a rational way to begin is with the piston launcher loss factor. This can be iterated until the initial driver pressure rise prior to diaphragm rupture, which is unaffected by downstream flow processes, closely matches the experimental driver pressure. Following diaphragm rupture, shock speeds in the driven tube are then used to establish the second loss factor. Once both loss factors are established, they are both further fine-tuned until the best agreement is obtained between L1d and experiment driver pressure traces and shock speeds. Final loss factors were, respectively, 2.25 and 6.25 at the piston launcher and primary diaphragm downstream location.

#### 6.4 Inviscid L1d simulation using driver equivalent temperature

Loss factors for the inviscid L1d model were applied at the same two locations as the viscous model. For the inviscid model, viscosity was disabled in the driven tube (secondary driver, test, and accelerator gas slugs), for two reasons. The first reason relates to spurious static pressures and temperatures which are observed with the viscous model; when viscosity is applied to a 1-D model, each cell is subject to continuous viscous heat transfer, which can modify cell temperatures significantly. While shock speeds may be tuned to match experiment, computed flow Mach numbers can become unrealistically low due to the artificially high temperatures. This is in contrast to the actual experiment, where viscous heat transfer is confined to the boundary layer, and the gas properties of the core flow remain largely unaffected. Furthermore, when viscosity is applied, a pressure gradient behind the shock wave develops in response to the added resistance presented by the shear stresses acting on the downstream flow; in reality the shear stresses reduce away from the wall, and the core flow is significantly less impeded. As a result, static pressure traces from viscous L1d models display a gradient which is not observed in the experiment.

The second reason for disabling the viscosity model relates to recent expansion tube analytical modelling with X2. The X2 analyses [7, 39] have shown that analytical techniques can closely predict shock speed through the *test* gas when equilibrium chemistry is accounted for and when the free-piston driver performance is effectively characterized.

These techniques do not account for viscous effects, indicating that viscosity does not play a significant role in the *shock* tube. Although viscous effects have fundamental importance in the low-pressure acceleration tube, these effects do not need to be captured by L1d, since the more physically correct 2-D axisymmetric analysis is used to reconstruct the test flow in this region of the machine.

Ideal gas isentropic relations are normally used to predict the driver gas temperature when the primary diaphragm ruptures, based upon the initial driver gas fill pressure and temperature, and the final rupture pressure. However, for reasons already noted in Sect. 6.2, there is usually a deficit between predicted and experimentally observed shock speeds. Reference [39] proposed a technique to calculate driver “effective” pressure and temperature based on experimentally measured shock speeds, that indirectly accounts for loss mechanisms in the driver and was shown to provide more accurate predictions of shock speed across a range of conditions (high and low enthalpy). Although this technique was proposed for analytical state-to-state calculations, where the driver is modelled as a fixed volume, it has now been adapted to a dynamic free-piston driver model for this study. Using a free-piston driver model ensures that complex longitudinal wave processes can be captured in the hybrid simulation scheme.

Since the piston trajectory fundamentally depends upon the driver pressure history, it is problematic to attempt to scale driver pressure in accordance with Ref. [39]; therefore, only temperature is scaled when piston dynamics are included. Assuming a rupture pressure of 17.5 MPa, Ref. [36] has previously calculated the “effective” temperature at rupture for condition x3-scr-m10p0a-rev-0. Based on an average experimental shock speed through the helium secondary driver of 3144 m/s, the effective temperature was computed to be 2407 K, which is much lower than the ideal isentropic temperature of 3745 K (for an initial temperature of 293 K). Given the compression ratio,  $\lambda = 45.7$ , this corresponds to an effective *fill* temperature as follows:

$$T_{4,i} = T_4/\lambda^{\gamma-1} = 2407 \text{ K}/\lambda^{(5/3-1)} = 188 \text{ K} \quad (2)$$

This is the fill temperature which, when specified for the L1d model, will result in a temperature of 2407 K once the driver pressure reaches 17.5 MPa and the primary diaphragm ruptures. There is no suggestion that this is a “real” temperature; Ref. [36] demonstrated that the driver fill temperature was close to the laboratory ambient temperature, as is normally assumed. Still, using an effective fill temperature is proposed as an alternative technique to account for the significant driver losses in the L1d model and offers several advantages.

Firstly, it preserves the L1d driver pressure calculation as a simulation validation metric. In turn, this should therefore



not significantly affect the piston dynamics in the L1d model, where the driver gas slug is modelled as a mixture of calorically perfect argon and helium. The wave speed in the driver gas *will* be reduced in the L1d simulation due to lower temperatures; however, this effect will only become prominent at the very end of the piston stroke, when the combination of high piston speed and short slug length makes compression waves evident. Furthermore, changes to wave speed will slightly alter the time sequence of piston pressure loading, but not the magnitude.

Scaling the driver fill temperature also contains losses to the driver gas, which successful application of driver effective properties in Refs. [7, 39] suggests is physically representative of the actual machine. This then avoids the use of a downstream viscosity model, which would otherwise produce spurious flow features in the expansion tube simulations, and reduces the dependence on pipe flow loss factors, which can fundamentally change the duct flow.

The inviscid L1d model was tuned against experiment using the same approach as for the viscous model. An initial driver temperature of 185 K was used (from early calculations prior to final publication of Ref. [36]). Loss regions were applied at the same spatial locations as the viscous model and were, respectively, equal to 8.0 and 3.7 at the launcher and driver area change (compared to 2.25 and 6.25 for the viscous model).

## 6.5 L1d simulation results

Figure 10 compares computed and experimental driver pressure traces for reference experiment x3s403. The pressure traces have been time-referenced to facilitate comparison. It can be seen that the inviscid 185 K model has marginally better agreement with experiment, although both models match closely. The discontinuity evident in the viscous L1d trace

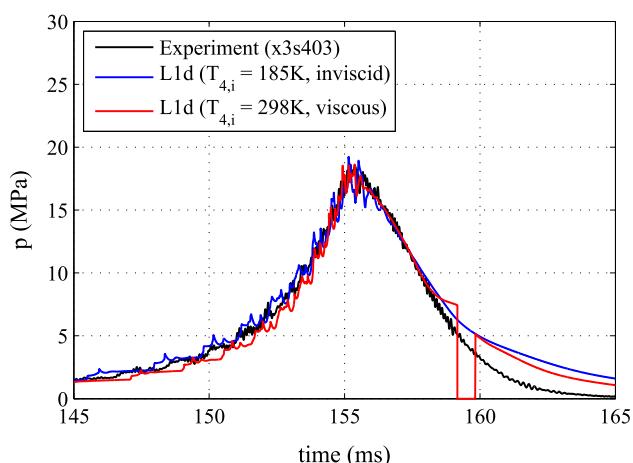


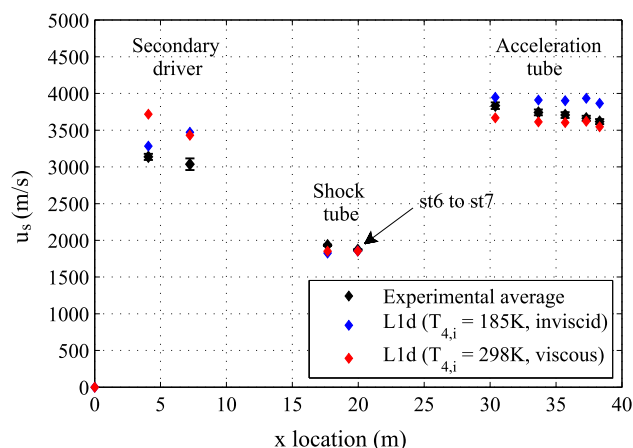
**Fig. 10** Comparison of experimental and computed driver pressures at transducer location ct

indicates that the piston is passing across the transducer location; however, this occurs well after diaphragm rupture. Between 158 and 165 ms, the experimental trace drops off more rapidly than either L1d model; this is likely to be due to a combination of both high-temperature effects and discharge of the piezoelectric PCB transducer over these comparatively long-duration events.

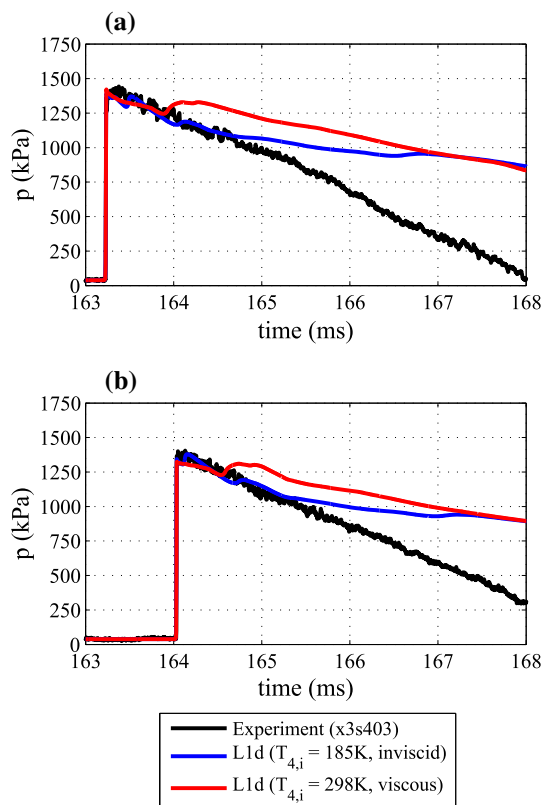
It is noted that there is some discrepancy in the high frequency response between the L1d models and the experiment. The L1d model cannot get the reflected wave timing exactly correct because of the requirement to model the duct with gradual area changes, instead of the abrupt changes present in the actual facility. This stretches out all of the tube area change sections and, towards the end of the piston stroke (when the gas slug length is shortest), the effect of this gradual duct approximation becomes more significant. This is a necessary modelling approximation which has a minor effect on the transmitted pressure pulse from the driver. It is also noted that because the L1d code maintains the coherence of wave processes, the effects of perturbations are expected to be stronger in the simulation than in the real facility.

Figure 11 compares shock speeds through the driven tube. The experimental shock speeds are averaged across six repeat experiments; error bars show the standard deviation between experiments and indicate excellent shot-to-shot repeatability. The error bars are shown only for the experimental (black) data points and are quite small in range. It can be seen that both L1d models achieve a similar match to the experiment through the secondary driver and shock tube. As expected, the tuning process has succeeded in achieving good agreement with experiment for both models at the fourth set of data points (st6 to st7 in the figure), where the 2-D axisymmetric inflow is recorded.

The shock speeds differ significantly through the acceleration tube. The inviscid L1d model matches experiment well



**Fig. 11** Comparison of experimental and computed L1d shock speeds along driven tube



**Fig. 12** Comparison of experimental and computed static pressures in the downstream shock tube. **a** st6 static pressure, **b** st7 static pressure

at the first data point, but increasingly over-estimates shock speeds towards the end of the tube. This is a predictable result since it does not include the effects of viscosity; in the hybrid analysis scheme (Fig. 5), these viscous effects are accounted for by the 2-D axisymmetric model. The viscous model under-estimates shock speeds throughout the entire acceleration tube, with the biggest discrepancy at the beginning of the tube and closer agreement towards the end of the tube.

While superficial agreement between the experimental results and both L1d simulations is demonstrated in Figs. 10 and 11, examination of the detailed flow properties reveals fundamental differences between the simulations.

Figure 12 compares L1d test gas static pressures at st6 and st7 in the shock tube to experiment x3s403. Results have been time-referenced to shock arrival of the inviscid L1d model. Both L1d simulations predict similar initial pressure rises due to the tuned shock speeds; however, a second discrete pressure rise (following the initial shock arrival) is observed in the viscous model. The inviscid model matches experiment for a longer duration before diverging after about 1.5 ms; however, no discrete pressure rises are observed.

Spurious effects from using a 1-D viscosity model become apparent in Fig. 13a–f. All results have been time-referenced

to shock arrival of the inviscid L1d model. Figure 13a–c compare computed and experimental static pressure traces at acceleration tube transducer locations at4, at6, and at8. The magnitudes of the initial pressure rises reflect the shock speed results in Fig. 11; the inviscid 185 K driver model over-estimates shock speed through the acceleration tube, and therefore, these static pressures rise to the highest initial magnitudes; the viscous 298 K model more closely estimates the experimental shock speed and therefore also more closely matches the experimental pressure rise. However, it can be seen that the viscous model pressure traces do not exhibit an initial period of steady pressure after shock arrival, which is observed in the experiment and the inviscid model. This is the pressure gradient referred to in Sect. 6.4, which arises in response to the cell shear stresses applied in the viscous model.

The inviscid L1d model produces pressure traces which conform to the ideal classical model for expansion tube flow processes: the initial pressure rise is associated with shock-processed accelerator gas passing the transducer location; the interface between accelerator and test gas slugs can be identified as the small “blip” in the steady pressure region (and referring to Fig. 13d–f, a very clear drop in temperature). The useful test gas lies in the region between this “blip” and the eventual pressure rise from arrival of the unsteady expansion. As expected, the inviscid L1d model has a longer duration of approximately uniform pressure flow, since it does not account for boundary layer effects which are fundamentally important to expansion tube flow processes, but are later accounted for in the 2-D axisymmetric model.

Figure 13d–f compare computed temperatures at these three transducer locations (no experimental temperature measurements were made). Once more the inviscid model produces results typical of classical expansion tube flow: the initially low-pressure accelerator gas is uniformly heated to a very high temperature ( $\approx 4000$  K) after being compressed by the expanding test gas; the test gas itself has undergone a significant expansion and is now relatively cold ( $\approx 600$  K, which will further be expanded to  $\approx 300$  K through the nozzle).

The viscous L1d model produces an erroneous temperature history at each acceleration tube transducer location. The temperature begins to drop immediately following the sharp initial temperature rise associated with shock arrival. This temperature drop occurs due to heat loss from the hot accelerator gas to the cold wall. In the actual experiment, viscous effects are confined to the boundary layer, and the core flow temperature would not demonstrate this temperature drop. It is also noted that the length of the viscous accelerator gas slug is also shorter, due to the gas being colder and therefore more dense.

The viscous L1d model estimates a higher temperature test flow than the inviscid model. This occurs because the

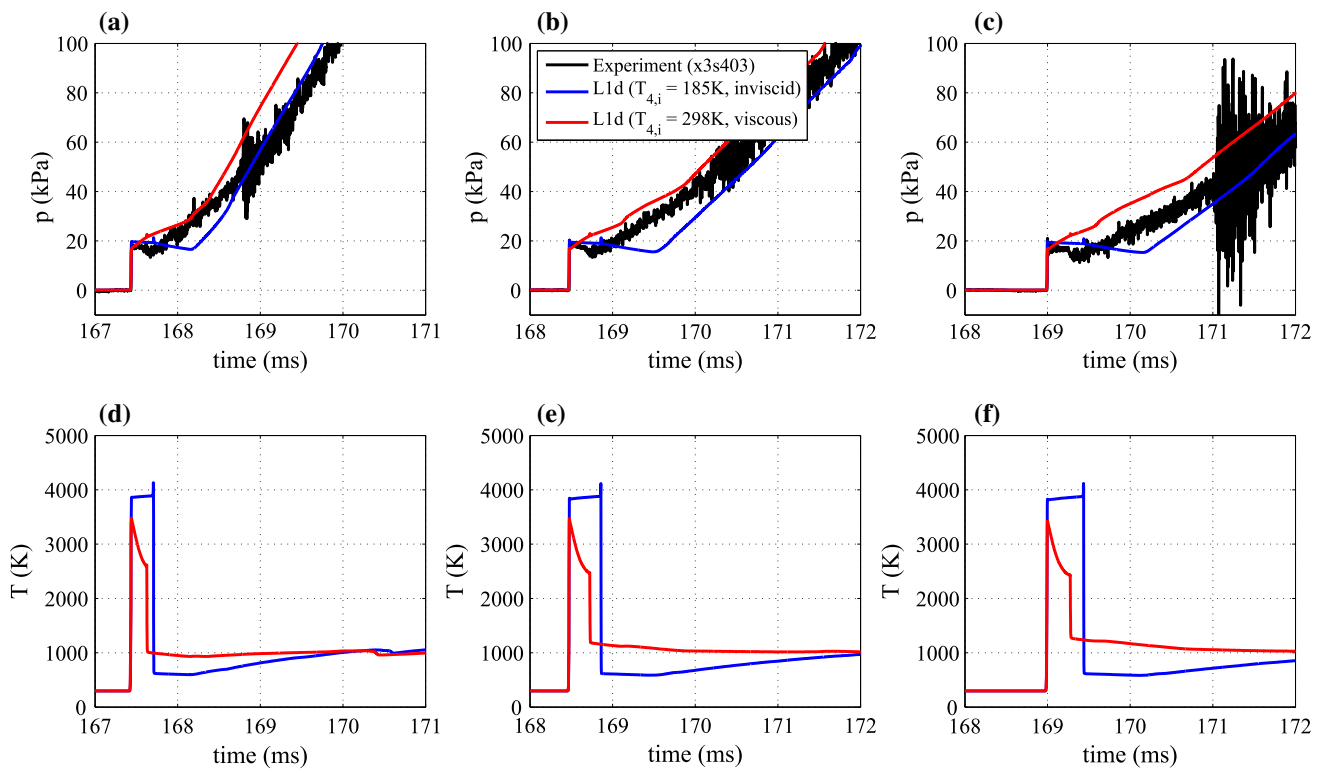


**Fig. 13** Comparison of computed and experimental static pressures (a–c), and computed temperatures (d–f), at acceleration tube transducer locations at4, at6, and at8. **a** at4 static pressure. **b** at6 static pressure.

**c** at8 static pressure. **d** at4 computed temperature. **e** at6 computed temperature. **f** at8 computed temperature

viscous shear stresses have limited the test gas expansion. Eventually both viscous and inviscid L1d models predict a similar temperature; in the inviscid model this corresponds to the unsteady expansion passing the transducer locations, where the test gas has not expanded fully and is therefore hotter.

The results of this detailed comparison of viscous and inviscid L1d models demonstrate that replicating the experimental shock speeds in a numerical model does not guarantee that the computed flow processes are sensible. The viscous model over-estimates the driver performance, however, shock speeds agree with experiment because the viscous stresses then slow down the flow. This is one non-physical process cancelling out another and, upon closer examination, produces incorrect static pressure and temperature profiles.

It is finally noted that both L1d models make use of loss regions at the piston launcher and the driver area change. This is considered necessary and acceptable at the piston launcher, since the primary purpose of this part of the model is to accelerate the piston to the required peak speed. However, the effect of the loss factor is more complex at the driver area change, and the effects on flow processes are uncertain. Figure 14 shows an  $x-t$  wave diagram with the log of static

pressure mapped over it, for the inviscid model, which reveals the complexity of even the 1-D wave processes. The driver area change loss factor is evident as a lighter shaded region of pressure loss immediately downstream of the driver (approximately located at  $x = 0$  m and  $t = 156$  ms). Although it was not attempted in this study, it is proposed that this loss factor could be removed entirely by further fine-tuning the driver effective fill temperature (185 K for this model). Scaling driver fill temperature has been shown in this paper to be an effective way to correct driver performance without introducing spurious effects in the downstream tube.

Now that the 1-D analysis has been completed, the transient flow towards the end of the shock tube may be used to “drive” a higher fidelity acceleration tube simulation.

## 7 Equilibrium gas assumption

As noted in Sect. 4, an equilibrium gas model was used for both the L1d simulations discussed in the present paper, as well as for the 2-D axisymmetric simulations detailed in the Part 2 companion paper [20]. This section considers the suitability of this equilibrium gas assumption, which depends upon the timescales of the axial wave processes in relation to

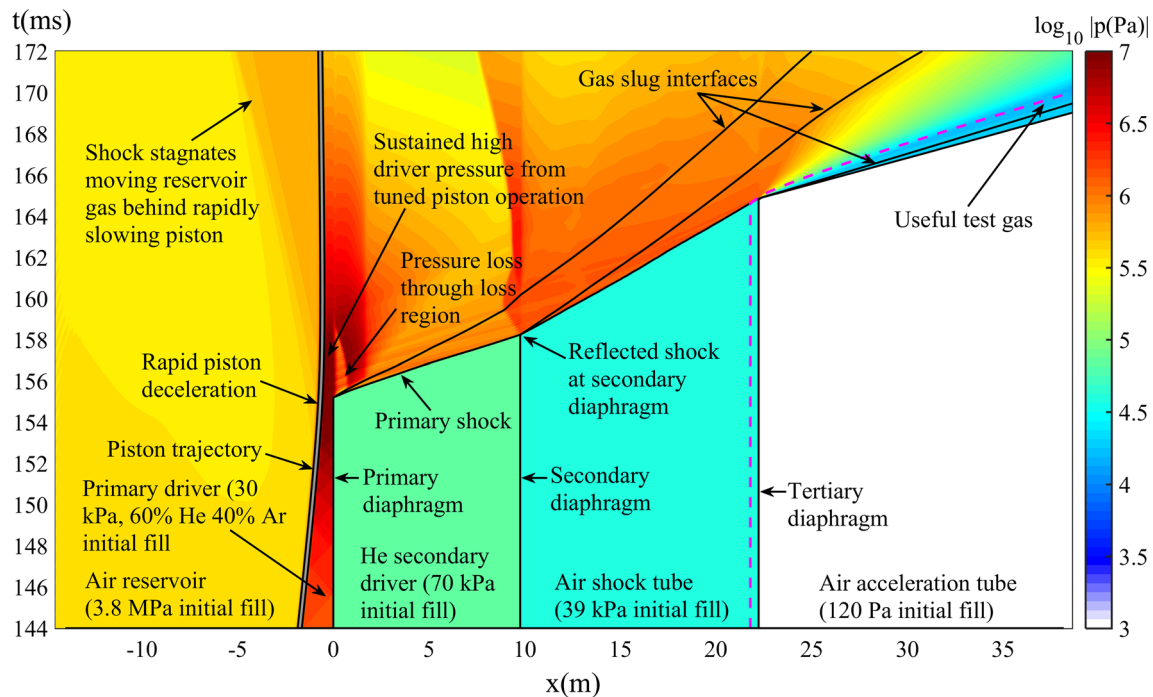


**Fig. 14**  $x-t$  wave diagram for L1d inviscid model, showing longitudinal wave processes. Contours represent the log of static pressure. Dashed magenta line shows the trajectory of an L1d Lagrangian cell of test gas originating at  $x = 21.8$  m in the shock tube

the thermochemical kinetic processes. Since the L1d simulations accurately capture axial wave processes, an assessment of the equilibrium assumption for the 1-D simulations can also be considered applicable to the 2-D axisymmetric simulations in Part 2.

Considering each of the five distinct regions of gas in the inviscid L1d expansion tube simulation, approximate temperature limits are as follows:

1. Air reservoir: 298–200 K (expansion from initially ambient temperature).
2. Helium/argon primary driver: 185–2400 K (or 298–3745 K for the viscous L1d model).
3. Helium secondary driver: 298–1700 K (after processing from both primary and reflected shocks).
4. Air test gas: 298–1800 K (after processing by primary shock).
5. Air accelerator gas: 298–3870 K (after processing by primary shock).

Within these temperature limits, the air reservoir and monatomic gas primary and secondary drivers can be accurately modelled as calorically perfect gases. The strongest chemical effects occur in the air accelerator gas; at approximately 4000 K this air will be vibrationally fully excited, and the  $O_2$  will be almost completely dissociated. While finite rate chemistry is likely to influence the accelerator gas properties, it is not necessary to capture these effects in the

simulations. This is permissible because the purpose of the accelerator gas is to control the degree of expansion of the test gas, which depends primarily on the accelerator gas density. Since the useful flow experiment in the test section does not begin until this hot gas is cleared from the test section, any discrepancies between its true properties and those predicted by the equilibrium model are relatively unimportant to the test gas characterization.

In the L1d simulation, the test gas is initially shock-processed to approximately 1800 K at 1400 kPa, before undergoing an unsteady expansion to the nozzle inlet conditions of approximately 600 K and 16 kPa. There will be essentially no dissociation of the test gas due to the relatively low shock speed and moderate temperatures up to 1800 K, but vibrational excitation will be significant. Across the unsteady expansion, if the vibrational relaxation timescales are comparable to the unsteady expansion timescales, then there is potential for freezing of the vibrational energy which will be unaccounted for by the equilibrium chemistry in the numerical simulations.

To assess the importance of thermal non-equilibrium with respect to the final test gas properties, the time history of an L1d cell of test gas was examined. Referring to Fig. 14, the dashed magenta line shows the trajectory of an L1d Lagrangian cell of test gas originating at  $x = 21.8$  m. It can be seen that the test gas from this region of the shock tube is the gas which is eventually processed to the final nozzle inlet condition, identified as “Useful test gas” in the figure. The



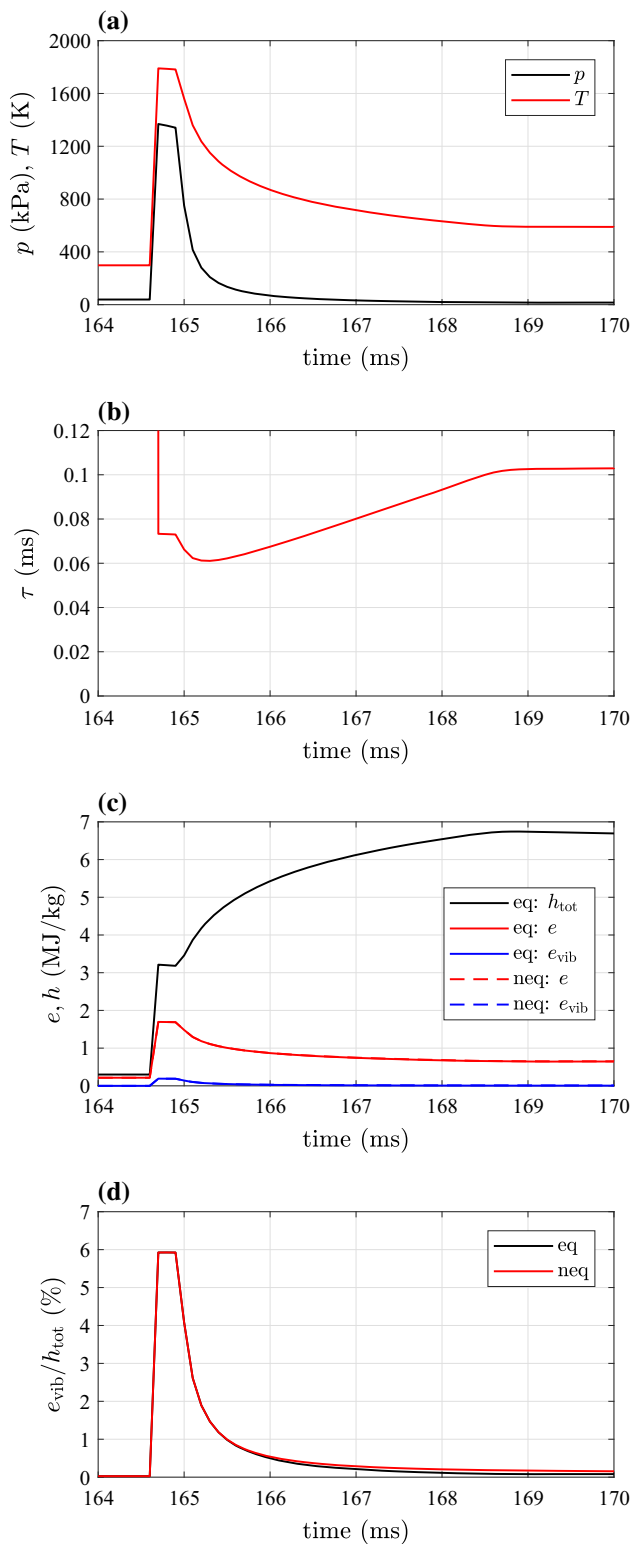


**Fig. 15** Flow property history for test gas cell originating at  $x = 21.8$  m from inviscid L1d model. **a** L1d cell gas properties. **b** Vibrational relaxation time. **c** Computed enthalpy and energy. **d** Vibrational energy and fraction

temperature and pressure history of this gas cell are presented in Fig. 15a, and it is noted that approximately 5.5 ms pass from initial shock processing to arrival at the nozzle inlet.

In the present context, the consequence of using an equilibrium chemistry model is to implicitly assume that vibrational relaxation timescales are much shorter than the flow timescales. This assumption can be tested by examining the vibrational relaxation rates of air. Sebacher and Guy [40] make a distinction between relaxation times in “expanding” flows and “compressing” shock tube flows, noting that relaxation is up to two orders of magnitude faster in the expanding flows. Comparing these two types of vibrational relaxation, it is considered appropriate to model the expansion tube test gas as an expanding flow, since the dominant test gas flow process is an unsteady expansion.

Equation (3), which is equation (14) from [40], shows the vibrational relaxation time,  $\tau$  (s), for the “expanding” air case.  $\tau$  is a function of temperature,  $T$ , (K) and pressure,  $p$ , (atm). This relaxation equation was applied to the pressure and temperature histories shown in Fig. 15a, giving the instantaneous vibrational relaxation time history shown in Fig. 15b.

$$\tau \cdot p = 1.2 \times 10^{-10} e^{130T^{-1/3}} \quad (3)$$

A thermal relaxation calculation utilizing Equation (3) was performed for the Fig. 15a  $p$ – $T$  history. Figure 15c compares the total internal energy,  $e$ , to the vibrational component,  $e_{vib}$ , for equilibrium (eq) and non-equilibrium (neq) cases. The equilibrium total enthalpy of the flow,  $h_{tot}$ , is also shown. It can be seen that  $e_{vib}$  (curves coloured blue) is insignificant compared to  $h_{tot}$  by the end of the unsteady expansion, and on the scale shown, equilibrium and non-equilibrium results are indistinguishable.

To facilitate detailed comparison of  $e_{vib}$ ,  $e_{vib}/h_{tot}$  is plotted in Fig. 15d. This plot confirms that equilibrium and non-equilibrium vibrational energies almost exactly match during the entire flow history of the test gas cell. This suggests that there is negligible frozen vibrational energy and it is appropriate to use the equilibrium thermochemical model.

## 8 Discretization error

The effect of discretization was assessed by uniformly scaling the cell count for both inviscid and viscous models. Models comprising 1000, 2000, 4000, and 8000 cells were compared, where 4000 cells was the nominal L1d cell count used in this study. Since the purpose of the 1-D analysis was to compute a transient inflow at the st6 transducer location, flow properties at this location are used for the present analysis.

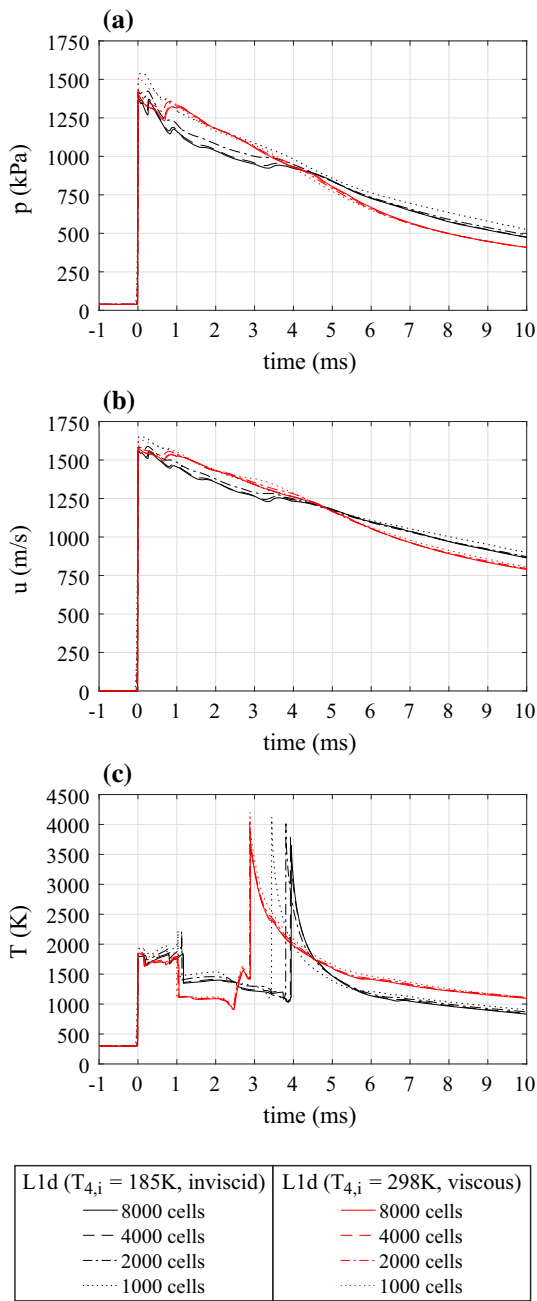


**Fig. 16** Test gas flow properties at st6 transducer location. **a** Static pressure at st6. **b** Velocity at st6. **c** Temperature at st6

Figure 16 shows the transient flow history at st6 for the four different cell counts. The curves are time-referenced for shock arrival at  $t = 0$ . 10ms of flow history after shock arrival are presented, since this is the duration of inflow that was later applied to the 2-D axisymmetric model, in the second stage of the hybrid CFD analysis. For both inviscid and viscous models, it can be seen that transient features in the plots collapse to the same curve for the 4000- and 8000-cell grids, indicating that the nominal 4000-cell model accurately captures the timing of transient phenomena.

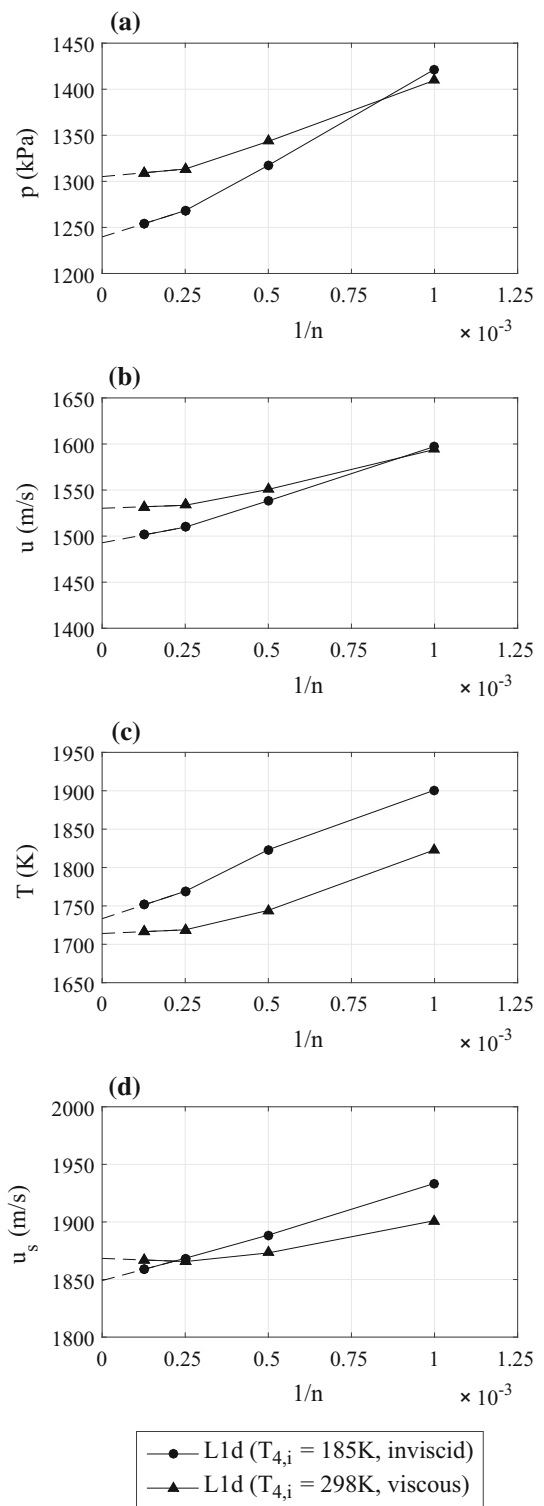


**Fig. 17** Time-averaged test gas flow properties. **a** Average pressure at st6. **b** Average velocity at st6. **c** Average temperature at st6. **d** Shock speed between st6 and st7

In Fig. 16, the test gas is observed to pass st6 for approximately the first millisecond, after which cooler expanded secondary driver helium arrives. Figure 17a–c plot the time-

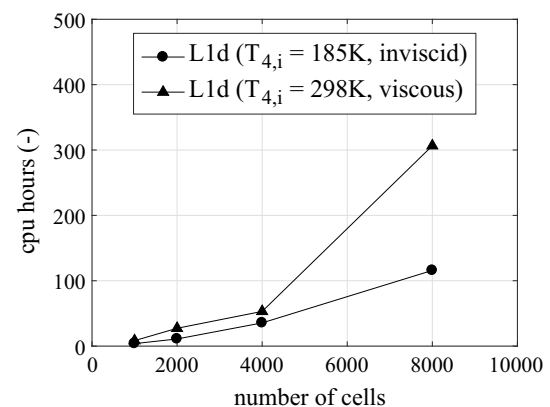
**Table 2** Average test flow properties at st6;  $\infty$  values are linearly interpolated for  $n = \infty$ 

$n$	$u_{s, \text{st6-7}}$ (m/s)	$u_{\text{av}}$ (m/s)	$p_{\text{av}}$ (kPa)	$T_{\text{av}}$ (K)
L1d ( $T_{4,i} = 185$ K, inviscid)				
1000	1934 (+4.6%)	1.422 (+14.7%)	1597 (+7.0%)	1901 (+9.7%)
2000	1889 (+2.2%)	1.317 (+6.2%)	1538 (+3.0%)	1823 (+5.2%)
<b>4000</b>	<b>1869 (+1.1%)</b>	<b>1.268 (+2.3%)</b>	<b>1510 (+1.1%)</b>	<b>1769 (+2.1%)</b>
8000	1859 (+0.5%)	1.254 (+1.1%)	1501 (+0.5%)	1751 (+1.0%)
$\infty$	1849	1.240	1493	1733
L1d ( $T_{4,i} = 298$ K, viscous)				
1000	1901 (+1.8%)	1.410 (+8.0%)	1594 (+4.2%)	1823 (+6.4%)
2000	1873 (+0.3%)	1.343 (+2.9%)	1551 (+1.4%)	1744 (+1.8%)
<b>4000</b>	<b>1866 (-0.1%)</b>	<b>1.313 (+0.6%)</b>	<b>1534 (+2.6%)</b>	<b>1719 (+0.3%)</b>
8000	1867 (-0.1%)	1.309 (+0.3%)	1532 (+0.1%)	1717 (+0.2%)
$\infty$	1868	1.305	1530	1714

averaged properties of this test gas (static pressure, velocity, and temperature, respectively) across the first millisecond after shock arrival, versus  $1/n$ , where  $n$  is the cell count. An exponentially decaying convergence is observed. For each plot, a dashed line has been extrapolated from the straight line joining the 4000 and 8000 cell data points, to  $1/n = 0$ , which represents an infinite cell count. The intercept of this dashed line with  $1/n = 0$  provides a conservative estimate of the fully converged value. The maximum discretization errors for each model have been calculated in terms of the percentage difference of each time-averaged flow property from the projected  $1/n = 0$  value and are presented in Table 2. The bold values for  $n = 4000$  cells indicate the estimated error for the nominal solution.

Referring to Table 2, it can be seen that the maximum discretization error for the nominal (4000 cell) inviscid model is 2.3% for the average velocity; for the viscous model, the maximum error is 2.6% for the static pressure. However, this discretization error is partially offset by the model tuning process. Referring to Fig. 17d, the average shock speed between st6 and st7 has been plotted versus  $1/n$ . It can be seen that for the 4000-cell model ( $1/n = 0.25 \times 10^{-3}$ ), the same shock speed is predicted by both viscous and inviscid models. This arises due to the tuning process, which ensures the true shock speed is predicted by both models. Therefore, while the 4000-cell models are not fully converged, they predict the true shock speed, and the tuning process would be expected to similarly correct the associated post-shock flow properties.

The L1d tuning process is iterative and can require calculation of many dozens of simulations. Although each L1d simulation is computationally cheap in relation to 2-D axisymmetric CFD, the simulations take place on a single processor and can become time-consuming for high cell counts and long simulation times. Figure 18 shows the computation time for the viscous and inviscid models with

**Fig. 18** Calculation time for different grid densities

different cell counts. Calculations were run on a Dell R820 server with  $4 \times 8$  core CPUs (Intel Xeon E5-4620 v2 @ 2.60 GHz). The nominal 4000 cell count was selected for this study because it can solve within approximately 2 days (36 h for the inviscid model; 53 h for the viscous model). Referring to Fig. 18, the calculation time increases significantly for the 8000-cell model (116 and 307 CPU hours for inviscid and viscous models, respectively) and was considered impractically long for this study.

## 9 Conclusion

This paper reports on the quasi-one-dimensional modelling of a free-piston driven expansion tube, using the L1d code, for use as the first stage of a hybrid CFD analysis of the facility. The L1d model was tuned to achieve agreement between the L1d and experimental shock speed across tube wall transducer pair st6 and st7, since these are the most downstream transducers before the acceleration tube begins. The L1d flow history at st6 was then used to calculate a transient inflow for

a higher-fidelity 2-D axisymmetric model of the low-density acceleration tube, nozzle, and test section, which is presented in the Part 2 companion paper [20].

Two key findings have arisen in the current paper: Firstly, L1d, which does not include direct physical models of loss mechanisms in the primary driver and across the area change, provides an excellent estimate of the driver pressure history, but will tend to over-estimate the primary driver performance. An effective way to scale the driver performance so that the driven shock speed matches experiment, without introducing undesirable non-physical downstream flow features, is to scale the initial driver fill temperature.

Secondly, in the actual facility, the gas core flow is partially decoupled from tube wall effects. It is therefore recommended that a viscous model should not be used in the 1-D CFD code, since this will normally involve averaging across the entire tube duct area, thereby introducing non-physical effects. Sections of the expansion tube facility where viscous effects become prominent should be modelled in 2-D.

This concludes the quasi-one-dimensional analysis applied to the full facility. Part 2 of this series [20] completes the hybrid analysis procedure, which couples the L1d simulation results at the end of the shock tube to an axisymmetric simulation of the acceleration tube, nozzle, and test section.

**Acknowledgements** The authors wish to thank Frans De Beurs, Neil Duncan, and the EAIT Faculty Workshop, for technical assistance with X3; The Australian Research Council for support and funding; The Queensland Smart State Research Facilities Fund 2005 for support and funding; The Australian Space Research Program and UQ for their funding in support of the “Scramjet-based Access-to-Space Systems” (SCRAMSPACE) project; The UQ High Performance Computing (HPC) Support Group for supercomputing support; this work was supported by computational resources provided by the Australian Government through Raijin and Magnus under the National Computational Merit Allocation Scheme.

## References

- Morgan, R.: Development of X3, a superorbital expansion tube. In: AIAA 38th Aerospace Sciences Meeting and Exhibit, 10–13 January, Reno, NV, AIAA Paper 2000-558 (2000). <https://doi.org/10.2514/6.2000-558>
- Ponce, J.S.: Scramjet testing at high total pressure. PhD Thesis. School of Mechanical and Mining Engineering, The University of Queensland, St Lucia, Australia (2016). <https://doi.org/10.14264/uq.12016.71>
- Toniato, P., Gildfind, D., Jacobs, P., Morgan, R.: Current progress of the development of a Mach 12 scramjet operating condition in the X3 expansion tube. In: The 20th Australasian Fluid Mechanics Conference, 5–8 December, Perth, Australia (2016)
- Gildfind, D., Sancho, J., Morgan, R.: High Mach number scramjet test flows in the X3 expansion tube. In: Bonazza, R., Ranjan, D. (eds.) 29th International Symposium on Shock Waves 1, vol. 1, pp. 373–378. Springer, Dordrecht (2015). [https://doi.org/10.1007/978-3-319-16835-7\\_58](https://doi.org/10.1007/978-3-319-16835-7_58)
- Gildfind, D., Morgan, R., McGilvray, M., Jacobs, P.: Production of high Mach number scramjet flow conditions in an expansion tube. AIAA J. **52**(1), 162–177 (2014). <https://doi.org/10.2514/1.J052383>
- Gildfind, D., Morgan, R., Jacobs, P.: Expansion tubes in Australia. In: Igra, O., Seiler F. (eds.) Experimental Methods of Shock Wave Research, vol. 4, Chap. 1, pp. 399–431. Springer, Basel (2016). [https://doi.org/10.1007/978-3-319-23745-9\\_13](https://doi.org/10.1007/978-3-319-23745-9_13)
- Gildfind, D., James, C., Toniato, P., Morgan, R.: Performance considerations for expansion tube operation with a shock-heated secondary driver. J. Fluid Mech. **777**, 364–407 (2015). <https://doi.org/10.1017/jfm.2015.349>
- Paull, A., Stalker, R.: Test flow disturbances in an expansion tube. J. Fluid Mech. **245**, 493–521 (1992). <https://doi.org/10.1017/S0022112092000569>
- Morgan, R.: Free-piston driven expansion tubes. In: Ben-Dor, G., Igra, O., Elperin, T. (eds.) Handbook of Shock Waves, vol. 1, Chap. 4.3, pp. 603–602. Elsevier, San Diego (2001). <https://doi.org/10.1016/B978-012086430-0/50014-2>
- Miller, C.: Operational experience in the Langley expansion tube with various test gases, NASA Technical Memorandum 78637. NASA Langley Research Center, Hampton (1977)
- Morgan, R., Stalker, R.: Double diaphragm driven free piston expansion tube. In: 18th International Symposium on Shock Waves, 21–26 July, Sendai, Japan (1991)
- Jacobs, P.: Numerical simulation of transient hypervelocity flow in an expansion tube. Comput. Fluids **23**(1), 77–101 (1992). [https://doi.org/10.1016/0045-7930\(94\)90028-0](https://doi.org/10.1016/0045-7930(94)90028-0)
- Neely, A., Morgan, R.: The superorbital expansion tube concept, experiment and analysis. Aeronaut. J. **98**, 97–105 (1994). <https://doi.org/10.1017/S0001924000050107>
- Chan, W., Smart, M., Jacobs, P.: Experimental validation of the T4 Mach 7.0 nozzle. Technical Report 2014/14. School of Mechanical and Mining Engineering, The University of Queensland, St Lucia (2014)
- Hannemann, K., Karl, S., Schramm, J., Steelant, J.: Methodology of a combined ground based testing and numerical modelling analysis of supersonic combustion flow paths. Shock Waves **20**, 353–366 (2010). <https://doi.org/10.1007/s00193-010-0269-8>
- Gildfind, D., Morgan, R., Sancho, J.: Design and commissioning of a new lightweight piston for the X3 expansion tube. In: Bonazza, R., Ranjan, D. (eds.) 29th International Symposium on Shock Waves 1, vol. 1, pp. 367–372. Springer, Dordrecht (2015). [https://doi.org/10.1007/978-3-319-16835-7\\_57](https://doi.org/10.1007/978-3-319-16835-7_57)
- Gildfind, D.: Development of high total pressure scramjet flow conditions using the X2 expansion tube. PhD Thesis. School of Mechanical and Mining Engineering, The University of Queensland, St Lucia (2012)
- Gordon, S., McBride, B.: Computer program for complex chemical equilibrium compositions and applications. NASA RP-1311. NASA Lewis Research Center, Cleveland (1994)
- Pinckney, S.: A short static-pressure probe design for supersonic flow, NASA TN D-7978. NASA Langley Research Center, Hampton (1975)
- Gildfind, D.E., Jacobs, P.A., Morgan, R.G., Chan, W.Y.K., Gollan, R.J.: Scramjet test flow reconstruction for a large-scale expansion tube, Part 2: hybrid CFD analysis. Shock Waves. <https://doi.org/10.1007/s00193-017-0786-9>
- PCB Piezotronics Inc.: Product specification for PCB(R) 112A22 ICP(R) pressure sensor. <https://www.pcb.com/products.aspx?m=112A22>. Downloaded 21 Jan 2017
- Kulite Semiconductor Products, Inc.: Product specification for Kulite(R) XTEL-190 (M) series pressure sensor. [www.kulite.com/docs/products/XTEL-190.pdf](http://www.kulite.com/docs/products/XTEL-190.pdf). Downloaded 21 Jan 2017
- Gollan, R., Jacobs, P.: About the formulation, verification and validation of the hypersonic flow solver Eilmer. Int. J. Numer. Methods Fluids **73**, 19–57 (2013). <https://doi.org/10.1002/flid.3790>



24. Jacobs, P.: Quasi-one-dimensional modeling of a free-piston shock tunnel. *AIAA J.* **32**(1), 137–145 (1994). <https://doi.org/10.2514/3.11961>
25. Mirels, H.: Test time in low-pressure shock tubes. *Phys. Fluids* **6**(9), 1201–1214 (1963). <https://doi.org/10.1063/1.1706887>
26. Mirels, H.: Shock tube test time limitation due to turbulent-wall boundary layer. *AIAA J.* **2**(1), 84–93 (1963). <https://doi.org/10.2514/3.2218>
27. Wendt, M., Macrossan, M., Jacobs, P., Mee, D.: Pilot study for a rarefied hypervelocity test facility. In: 13th Australasian Fluid Mechanics Conference, 13–18 December, Monash University, Melbourne, Australia (1998)
28. Wheatley, V., Chiu, H., Jacobs, P., Macrossan, M., Mee, D., Morgan, R.: Rarefied, superorbital flows in an expansion tube. *J. Numer. Methods Heat Fluid Flow* **14**(4), 512–537 (2004). <https://doi.org/10.1108/09615530410532277>
29. Jacobs, P., Silvester, T., Morgan, R., Scott, M., Gollan, R., McIntyre, T.: Superorbital expansion tube operation: estimates of flow conditions via numerical simulation. In: 43rd AIAA Aerospace Sciences Meeting and Exhibit, 10–13 January, Reno, Nevada, AIAA Paper 2005-0694 (2005). <https://doi.org/10.2514/6.2005-694>
30. Morgan, R., McIntyre, T., Jacobs, P., Buttsworth, D., Macrossan, M., Gollan, R., Capra, B., Brandis, A., Potter, D., Eichmann, T., Jacobs, C., McGilvray, M., van Diem, D., Scott, M.: Impulse facility simulation of hypervelocity radiating flows. In: Wilson, A. (ed.) Proceedings of the 2nd International Workshop on Radiation of High Temperature Gases in Atmospheric Entry. ESA Publications, Noordwijk (2006)
31. Potter, D., Gollan, R., Eichmann, T., McIntyre, T., Morgan, R., Jacobs, P.: Simulation of CO<sub>2</sub>-N<sub>2</sub> expansion tunnel flows for the study of radiating shock layers. In: 6th AIAA Aerospace Sciences Meeting and Exhibit, 7–10 January, Reno, Nevada, AIAA Paper 2008-1280 (2008). <https://doi.org/10.2514/6.2008-1280>
32. Gildfind, D., Morgan, R., McGilvray, M., Jacobs, P., Stalker, R., Eichmann, T.: Free-piston driver optimisation for simulation of high Mach number scramjet flow conditions. *Shock Waves* **21**(6), 559–572 (2011). <https://doi.org/10.1007/s00193-011-0336-9>
33. The compressible-flow CFD project. The University of Queensland, St Lucia. <http://cfcfd.mechmining.uq.edu.au>
34. Jacobs, P.: An approximate Riemann solver for hypervelocity flows. *AIAA J.* **30**(10), 2558–2561 (1992). <https://doi.org/10.2514/3.11264>
35. Jacobs, P.: Shock tube modelling with L1d. Research Report No. 13/98. School of Mechanical and Mining Engineering, The University of Queensland, St Lucia, Australia (1998)
36. Parekh, V., Gildfind, D., Lewis, S., James, C.: X3 expansion tube driver gas spectroscopy and temperature measurements. In: AIAA Australian-Asia Regional Student Conference. American Institute of Aeronautics and Astronautics (2015)
37. Mundt, C., Boyce, R., Jacobs, P., Hannemann, K.: Validation study of numerical simulations by comparison to measurements in piston-driven shock-tunnels. *Aerosp. Sci. Technol.* **11**, 100–109 (2007). <https://doi.org/10.1016/j.ast.2006.12.002>
38. McGilvray, M., Austin, J., Sharma, M., Jacobs, P., Morgan, R.: Diagnostic modelling of an expansion tube operating condition. *Shock Waves* **19**, 59–66 (2009). <https://doi.org/10.1007/s00193-009-0187-9>
39. Gildfind, D., James, C., Morgan, R.: Free-piston driver performance characterisation using experimental shock speeds through helium. *Shock Waves* **25**(2), 169–176 (2015). <https://doi.org/10.1007/s00193-015-0553-8>
40. Sebacher, D.I., Guy, R.W.: Vibrational relaxation in expanding N<sub>2</sub> and air, NASA TM X-71988. NASA Langley Research Center, Hampton (1974)